

# Sensitivity of high-resolution idealized simulations of thunderstorms to horizontal resolution and turbulence parametrization

A. Verrelle,\* D. Ricard and C. Lac

CNRM-GAME (CNRS-Meteo-France), Toulouse, France

\*Correspondence to: A. Verrelle, CNRM-GAME (CNRS-Meteo-France), 42 avenue G. Coriolis, 31057 Toulouse, France.  
E-mail: antoine.verrelle@meteo.fr

Idealized simulations of deep moist convection are performed with the Meso-NH model at kilometric scales to assess the impact of the horizontal grid spacing (4 km, 2 km, 1 km and 500 m) and turbulence scheme (one-dimensional (T1D) versus three-dimensional (T3D) turbulence). The simulations generate one cell which splits into two convective systems: a leftward-moving multicellular system and a rightward-moving supercell.

Objective criteria based on statistical properties and bulk quantities are examined for both systems to characterize the convection. They show that the accumulated rainfall and corresponding surface area increase with increasing resolution, as does the area covered by the updraughts, while the 90th quantile of the intensity of updraught cores decreases. The 4 km horizontal grid spacing is set apart, as it clearly under-resolves the convective motions, but the difference between 2 and 1 km horizontal resolutions is larger than between 1 km and 500 m, suggesting the beginning of convergence at 500 m. Also, 1 km appears to represent the deep convective structures more correctly than 2 km for a practical weather forecast of organized convective systems.

T3D induces more mixing and enhances the microphysical processes compared with T1D, producing larger amounts of cloud cover and precipitation. Also, the magnitude of the pressure anomaly on the southeastern flank of the supercell is stronger, accentuating the path curvature. The difference between T1D and T3D becomes perceptible at 2 km, pointing out the necessity to deal with horizontal turbulent fluxes at kilometric resolutions. Although a stronger numerical diffusion added to T1D allows the necessary damping to be introduced at the spectral energy tail, it removes a part of the physical mixing and still misses some variance at larger scales.

The ratio between resolved and total turbulent kinetic energy (TKE) decreases with increasing resolution for both T1D and T3D, which is unexpected. The main explanation is insufficient turbulent mixing inside convective clouds, more pronounced at coarser resolution, which is also confirmed by the vertical velocity spectra. At 500 m horizontal resolution, the subgrid TKE is mainly due to dynamical processes, with maxima located at the upper level of the convective systems in areas of stronger potential temperatures associated with downdraughts. However, thermal production is mostly negative, underlying the lack of entrainment at the cloud edges.

**Key Words:** turbulence; deep convective cloud; horizontal grid spacing; Meso-NH model

Received 1 July 2013; Revised 27 February 2014; Accepted 6 March 2014; Published online in Wiley Online Library 23 May 2014

## 1. Introduction

In recent years, the increase in computing power has enabled the advent of operational limited-area numerical weather prediction (NWP) models with horizontal grid spacings of the order of a few kilometres and most operational forecast centres now use or plan to use models at kilometre scale. For example, Deutscher Wetterdienst (DWD) has been using the COSMO-DE model at 2.8 km resolution since 2007 (Baldauf *et al.*, 2011), while the

Met Office has been using the UK Unified Model (UM) at 4 km resolution since 2007 (Davies *et al.*, 2005) and UK Variable resolution (UKV) model at 1.5 km resolution since 2011 (Lean *et al.*, 2008). The AROME-France convective scale model with 2.5 km horizontal grid spacing became operational at Météo-France at the end of 2008 (Seity *et al.*, 2011). The Japan Meteorological Agency (JMA) has been operating the Meso-Scale Model (MSM) covering Japan and its surrounding areas at 5 km resolution since 2006 (Saito *et al.*, 2006; Narita and Ohmori, 2007) and is also

developing the Local Forecast Model (LFM) with a horizontal grid spacing of 2 km (Hirahara and Ishimizu, 2011). The WRF model (Janjic, 2003; Skamarock and Klemp, 2008) is in operational use at the National Centers for Environmental Prediction (NCEP), the Air Force Weather Agency (AFWA) and other centres at 4 km resolution.

These non-hydrostatic models with grid spacings below 5 km are well suited to the simulation of mesoscale phenomena and, in particular, deep moist convection (Weisman *et al.*, 2008). As the horizontal resolution tends towards 1 km, much of the convective motion is explicitly resolved and parametrization of deep convection is no longer needed. Nevertheless, there is still debate about the precise limit of horizontal resolution for which convection parametrization is no longer necessary (Dirmeyer *et al.*, 2012). This limit is thought to be around 2.5–5 km depending on the organization of the convection. It is worth noting that, more than grid resolution, the effective resolution (as defined by Skamarock (2004)) is crucial for estimating whether a convective event is explicitly represented. Numerical implicit and explicit diffusion and subgrid-scale physical mixing are the main factors modifying the effective resolution of a NWP model (Takemi and Rotunno, 2003; Ricard *et al.*, 2013).

Additionally, for cloud-resolving resolution, it is not clear which spatial horizontal resolution is needed to obtain a satisfactory representation of deep moist convection. Subkilometre simulations of deep moist convection seem to improve the initiation of convection and the small-scale features of convective systems (Zhang and Zhang, 2012; Warren *et al.*, 2014). Many studies have focused on the sensitivity of horizontal resolution and subgrid parametrization to the explicit simulation of deep moist convection. Lean *et al.* (2008) have shown that the 4 km UM representation suffers from large convective cells and delays initiation, whereas the 1 km UM suffers from small cells becoming too numerous in some situations. Petch *et al.* (2002) studied the impact of horizontal resolution on the diurnal development of shallow and deep convection over land. They found that the triggering of convection at 2 km resolution led to a delay in the development of convection, whereas at higher resolution (125 m) the transport of moisture in the subcloud layer was better resolved and so the convective cloud evolution was closer to observations.

Redelsperger and Sommeria (1986) evaluated the relative importance of the various features of the subgrid-scale turbulence parametrization in a horizontal sensitivity study of idealized deep moist convection case modelling. They demonstrated that the effects of low resolution can be partially compensated for by an advanced subgrid turbulence parametrization.

The dominant mechanism for boundary-layer development is turbulence created by buoyancy gradients due to surface forcing and by the shear of the mean wind profile. Boundary-layer schemes have to take all these processes into account. At the mesoscale (from a few hundred kilometres to a few kilometres horizontal resolution), the turbulence scheme is usually quasi-one-dimensional in the vertical, as the coarse horizontal resolution cannot represent large gradients. Turbulence is taken to be an entirely subgrid physical process and the boundary layer is assumed to be horizontally homogeneous. When the most energetic eddies are resolved by the model, large eddy simulation (LES) models are suitable to simulate highly turbulent flows with three-dimensional (3D) turbulence schemes to represent horizontal gradients. At intermediate scales (i.e. between about 100 and 1000 m), the so-called *terra incognita* range (Wyngaard, 2004), only one part of the energy-containing turbulence scale is resolved, while the other part has to be parametrized. Turbulence schemes need to be evaluated in this range. Honnert *et al.* (2011) provided the ratio of subgrid to resolved parts for five variables at different scales in the grey zone of turbulence for a convective boundary layer. This ratio from LES gives a reference for evaluating parametrizations at kilometric scales. They showed, in particular, that the standard version of their mesoscale model produced too many resolved movements at intermediate scales

(typically 500 m) in the boundary layer, as the turbulence scheme did not represent the impact of the subgrid thermal sufficiently, whereas a mass-flux scheme led to an overestimation of the subgrid part.

Moreover, the boundary-layer turbulence parametrizations interact strongly with other physics and in particular with deep convection. At kilometre and sub-kilometre scales, Moeng *et al.* (2010) have shown that no gap exists between resolved and subgrid scales (SGS) in the energy spectrum related to deep convection and that much of the moisture is transported vertically by small-scale motions. They show that correlation between resolved and unresolved scales at 1 km resolution strongly affects the unresolved turbulent flux.

Bryan *et al.* (2003) conducted idealized simulations of squall lines with grid spacings of 1 km and 500, 250 and 125 m and demonstrated a lack of convergence of the statistical properties of convective systems with increasing resolution. They concluded that traditional LES closures could not be used to simulate deep moist convection realistically with a grid spacing of the order of 1 km. Also, for idealized simulations of squall lines, Bryan and Morrison (2012) have shown that changes in horizontal grid spacings (ranging from 4 to 0.25 km) have a greater impact than changes in the microphysical set-up. In particular, the amount of precipitation is reduced when 250 m grid spacing is used rather than 1 km grid spacing, due to more intense evaporation processes. Kharoutdinov *et al.* (2009) ran an LES of a deep tropical convective event with a grid spacing of 100 m as a benchmark simulation. Then they performed four more simulations with horizontal grid spacings of 200, 400, 800 and 1600 m with the same initial conditions as the control run. Convergence of statistical properties was found between the LES and the 200 m grid spacing run. Also, Parodi and Tanelli (2010) have shown that simulations with LES turbulent closure perform better than simulations with the mesoscale approximation for a case study of deep convection in the Intertropical Convergence Zone (ITCZ) in the *terra incognita* range of grid spacing.

Simulated supercells have been investigated by Adelman and Droege (2002). They demonstrated that high-resolution simulations (500 m grid spacing) of a supercell produced several occlusions, whereas low resolution (2 km grid spacing) did not allow a cyclic process. Furthermore, the authors showed that the percentage of resolved kinetic energy was higher for the run at low resolution, because the gradients were poorly resolved. Knowing that subgrid TKE is parametrized with resolved gradients, the production of subgrid TKE is not great enough at 2 km horizontal resolution. Fiori *et al.* (2009, 2010) conducted several simulations of a supercell convective system with the COSMO model. They focused on the uncertainty in the modelling of deep convection due to the effects of grid spacing (with horizontal resolution ranging from 1–0.2 km) and turbulent parametrizations (LES turbulent closure or mesoscale parametrization based on the boundary-layer approximation). They concluded that the uncertainties in the supercell structure and its trajectory were reduced when a grid spacing such as 0.2 km was used in combination with LES parametrization.

Although most of the studies agree on the necessity to run at sub-kilometric resolution to capture the basic structures of deep convection, it is still unclear whether these resolutions are sufficient to resolve intracloud motions and whether traditional subgrid turbulence parametrizations can represent the mixing at the cloud/environment interface correctly. Moreover, few studies compare 3D versus 1D turbulence approaches inside deep clouds. To handle these questions, it is necessary to rely on objective criteria based on the storm characteristics. These criteria are based on statistical properties, as in Kharoutdinov *et al.* (2009), or bulk quantities, as in Langhans *et al.* (2012). Considering the simplified atmospheric framework of the supercell used to study deep moist convective processes, it also seems important to include a multicellular system in the analysis, as dynamical characteristics are significantly different between supercellular and multicellular storms.

In this article, the impacts of horizontal resolution and subgrid 1D or 3D turbulence applied to deep moist convection of supercellular and multicellular thunderstorms are investigated with the Meso-NH research model, which can emulate the capacities of mesoscale meteorological models, cloud resolving models (CRM) and LES models (see Cuxart and Jiménez, 2007; Couvreux *et al.*, 2012, among others). It has also been shown in Ricard *et al.* (2013) that Meso-NH presents a good effective resolution of  $5-6\Delta x$  for deep convective cases at horizontal grid spacings between 2.5 km and 500 m.

This study addresses the following question: at what resolution is a 3D turbulence scheme necessary for good representation of convective systems? This is a crucial question for the next generation of NWP models as, for the moment, most operational models use 1D turbulence schemes (derived from LES closure or a 1D mesoscale approach). This study also aims to assess the turbulence inside convective clouds.

In the rest of the article, we first describe the initial conditions and model configuration used in this study. Then the features of convective systems for the reference simulation are presented in section 2. The sensitivity to the horizontal resolution inside clouds is discussed in section 3. Turbulence inside clouds is then analyzed and the benefit of using 3D turbulence evaluated in section 4. Conclusions and perspectives are discussed in section 5.

## 2. Model and experimental set-up

### 2.1. Model

We used the research non-hydrostatic model Meso-NH (Lafore *et al.*, 1997), which is based on the anelastic approximation of the pseudo-incompressible system of Durran (1989). It is a grid-point Eulerian model using a fourth-order centred advection scheme for the momentum components and the piecewise parabolic method (PPM) advection scheme Colella and Woodward (1984) for other variables, associated with the leap-frog time scheme. It uses a C-grid in the Arakawa convention (Mesinger and Arakawa, 1976) for both horizontal and vertical discretizations, with a conformal projection system of horizontal coordinates and a Gal-Chen and Somerville (1975) system of vertical coordinates. The model uses a fourth-order diffusion scheme on the momentum components only, to suppress very short wavelength modes. This diffusion operator is applied only to the fluctuations of the wind variables. The fluctuations are defined as the departures from the large-scale value.

Concerning the physical package, a mixed one-moment microphysical scheme is activated (Pinty and Jabouille, 1998). It is a three-class ice parametrization coupled to a Kessler scheme for warm processes. Thus, five prognostic variables of water condensates are considered: cloud droplets, rain, ice crystals, snow and graupel mixing ratios in addition to water vapour. A subgrid condensation scheme based on the turbulence parametrization following the Gamma probability distribution is used (Bougeault, 1982).

The turbulence scheme in the Meso-NH model was developed for both mesoscale applications and LES (Cuxart *et al.*, 2000) derived from Redelsperger and Sommeria (1986). The turbulence scheme is based on a complete subgrid scheme (noted SGS) with a 1.5-order closure coming from the system of second-order equations for the turbulent moments (see details in the Appendices).

For LES resolutions, the scheme is used in its complete three-dimensional formulation (called '3D turbulence') and the most energetic parametrized eddies are just a little smaller than the grid mesh: the Deardorff length-scale is used, corresponding to the grid size but limited by the stability. When the scheme is used at the mesoscale (horizontal grid sizes larger than 2 km), it can be assumed that the horizontal gradients and turbulent fluxes are much smaller than their vertical counterparts and can be neglected (called '1D turbulence'), so only vertical gradients

are taken into account (i.e. terms involving  $\partial/\partial x_1$  and  $\partial/\partial x_2$  are neglected in the equations in the Appendices, except for the advection term in Eq. (A1)). The mixing length is parametrized in a physical way at every level according to Bougeault and Lacarrere (1989). It is postulated that this mixing length  $L$  can be related to the distance that a parcel having a given TKE amount at level  $z$  can travel downward,  $l_{\text{down}}$ , or upward,  $l_{\text{up}}$ , before being stopped by buoyancy effects.

Thus, the BL89 mixing length is calculated only in the vertical direction. When it is used in T3D mode, the horizontal mixing length is taken to be equal to the vertical one. It is assumed that turbulence is isotropic, so the mixing length is the same in all three dimensions. That corresponds in fact to a 'quasi-3D' turbulence scheme.

Our simulations are performed with the BL89 mixing length both in T1D and T3D modes, as the horizontal resolution ranges from kilometric scale to intermediate scales, i.e. at a resolution coarser than the LES mode.

### 2.2. Experimental design and initial conditions

In this framework, idealized simulations of deep moist convection are performed at kilometric and sub-kilometric scales without a surface scheme, radiation scheme, orography or Coriolis force. Moreover, all the simulations are run with no deep convection parametrization or shallow convection scheme. The model is run on a 3D domain,  $300 \text{ km} \times 300 \text{ km}$  in horizontal area, with a vertical extension of 38 km. A stretched vertical grid is used, gradually varying from 4 m at the surface to 1000 m at 15 km and to 5500 m at 38 km. A Rayleigh layer with damping coefficient of maximum value  $0.01 \text{ s}^{-1}$  is set in the 18 highest kilometres to damp gravity waves in the stratosphere. Open radiative boundary conditions are used for outflow boundaries. Free slip conditions are assumed at the bottom boundary.

To trigger convection, an ellipsoidal thermal perturbation of maximum 2 K, with a horizontal radius of 10 km and a vertical radius of 1.4 km, is inserted in the low levels (the centre is placed at a height of 1.4 km), superimposed on a horizontally uniform barotropic initial state, the temperature, wind and humidity profiles of which come from the studies of Weisman and Klemp (1982, 1984). The profiles of temperature and moisture are based on the same analytic expressions given in Weisman and Klemp (1982) with a surface mixing ratio of  $14 \text{ g kg}^{-1}$ . The CAPE, calculated from the initial analytic profiles, is about  $1600-1700 \text{ J kg}^{-1}$  and indicates a conditionally unstable environment. This thermal perturbation is located at (60, 30 km) (represented by the black cross in Figure 1(a)) in the horizontal domain to optimize the trajectories of simulated convective systems and avoid the influence of boundaries. Wind profiles are initialized with a half-circle clockwise hodograph:  $u$  varies from zero at the surface to  $32 \text{ m s}^{-1}$  at 5 km above ground level (AGL),  $v$  varies from zero at the surface to  $15 \text{ m s}^{-1}$  at 2.5 km AGL and decreases to zero at 5 km AGL, while the horizontal wind remains constant and unidirectional above 5 km ( $u = 32 \text{ m s}^{-1}$ ,  $v = 0 \text{ m s}^{-1}$ ). The magnitude of the velocity variation along the arc of the curved hodograph between 0 and 5 km is  $U_s = 50 \text{ m s}^{-1}$ . This vertical wind profile and the unstable environment are propitious for the development of a right-moving supercell. It is worth noting that the same thermodynamic profiles are used in Fiori *et al.* (2010), but our simulation domain is four times larger, which allows the evolution of convective systems to be documented after 2 h.

Eight simulations were performed to assess sensitivity to horizontal resolution (4, 2 and 1 km and 500 m) and to the choice of turbulence scheme (T1D and T3D modes). The control experiment ran with 500 m horizontal grid spacing using the T3D scheme. For all these simulations, the numerical horizontal diffusion was kept the same, with an equivalent damping scale of 30 min for the  $2\Delta x$  waves.

A first additional simulation was performed with 500 m horizontal grid spacing without a turbulence scheme (500mNOT).

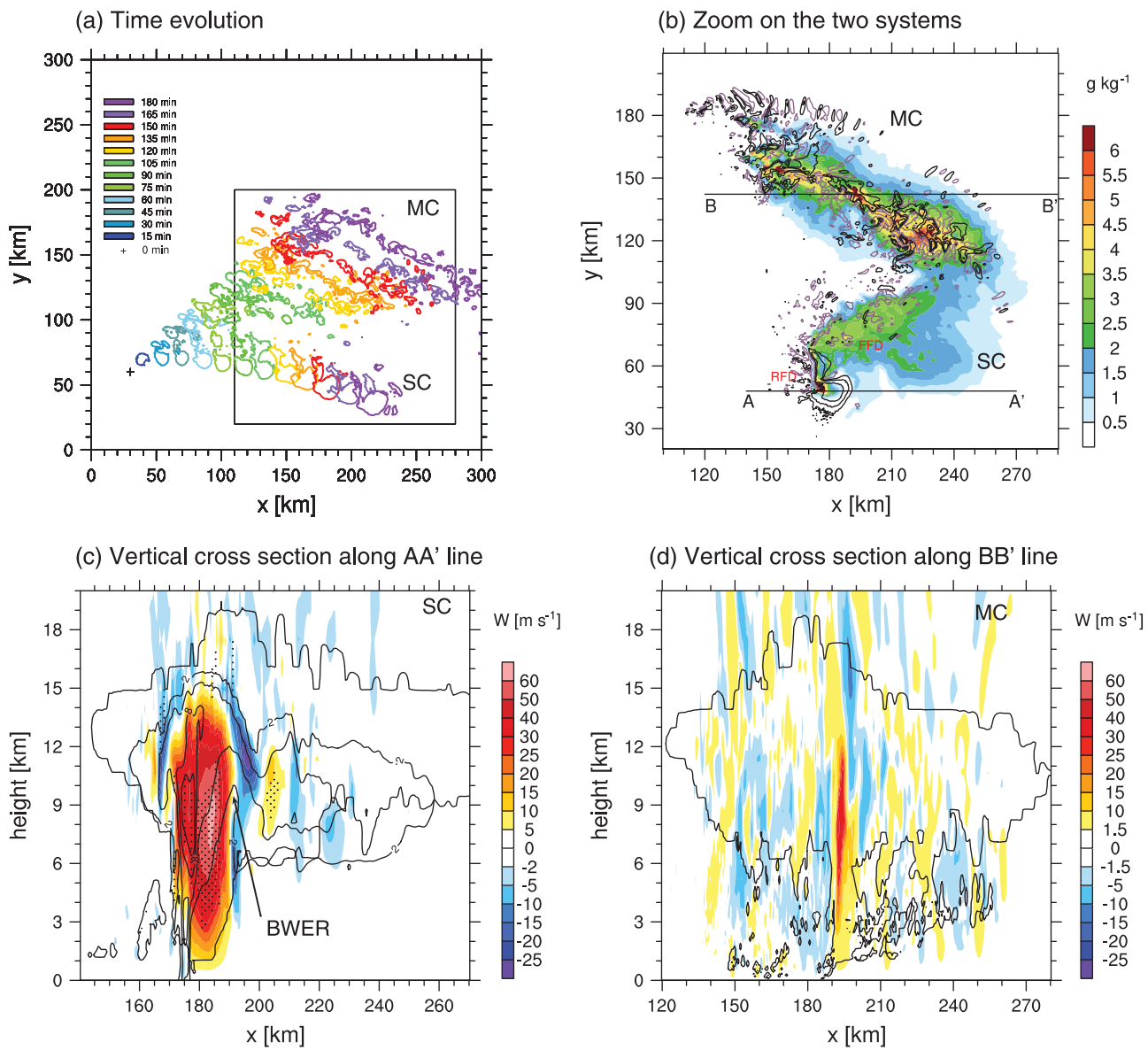


**Figure 1.** Control run (500mT3D). (a) Time evolution every 15 min of cloud contour ( $4 \text{ g kg}^{-1}$ , colour lines) at 5 km AGL. (b) Horizontal cross-section of both systems at 150 min: rain, graupel and snow ( $\text{g kg}^{-1}$ , colour shading) averaged between 2 and 7 km; positive (negative) vertical velocities are represented by black (red) contours of 2, 5 and 10  $\text{m s}^{-1}$  ( $-2 \text{ m s}^{-1}$ ) at 1 km AGL. Subdomain is indicated by the box in (a). (c) Vertical velocities along AA' (in b) ( $\text{m s}^{-1}$ , colour lines), sum of precipitating hydrometeors (2, 5, 8 and 10  $\text{g kg}^{-1}$ , grey lines), vertical vorticity ( $>0.01 \text{ s}^{-1}$ , stippling) and cloud contour (ice and cloud water mixing ratio:  $0.001 \text{ g kg}^{-1}$ , heavy black line). (d) Vertical velocities along BB' (in b) ( $\text{m s}^{-1}$ , colour shading) and cloud contour (ice and cloud water mixing ratio:  $0.001 \text{ g kg}^{-1}$ , heavy black line).

The mixing came only from the implicit diffusion of the advection schemes and from the numerical diffusion, which is identical to the previous simulations. In order to assess the impact of a stronger numerical diffusion with the T1D scheme, a second additional simulation (500mT1D-SD) was performed with strong diffusion (with an equivalent damping scale of 5 min for the  $2\Delta x$  waves). The model was integrated up to 3 h. The same time step of 2 s was used for all runs, in order to lead sensitivity tests on the horizontal resolution or the turbulence, keeping everything else constant. Moreover, the strong updraughts in the supercell prevented any significant increase of the time step at coarser resolutions, due to the vertical component of the local Courant number, as the vertical resolution was the same for all simulations (of the order of 200 m at 4 km height, where the vertical velocity of the supercell exceeded  $60 \text{ m s}^{-1}$ ).

### 3. Control run

Supercell thunderstorms are well known as one of the most dangerous types of convective storm, producing severe weather such as hail, tornadoes and wind damage. They are characterized by a single dominant updraught associated with low-level and

mid-level mesocyclones. In its mature phase, a supercell also has two downdraught areas: the forward-flank downdraught (FFD) and rear-flank downdraught (RFD) (Lemon and Doswell, 1979). The FFD, which is a thermodynamically driven process, is located below the precipitation area that occurs ahead of the main updraught. The RFD, located upwind of the main updraught, has both thermodynamical and dynamical origins. Hydrometeor loading/evaporation or sublimation are the thermodynamical basis for downdraught formation, whereas dynamical processes imply a vertical pressure gradient.

Numerical modelling has played an important role in improving our understanding of storm structure and development (Klemp and Wilhelmson, 1978). Two major parameters, the vertical shear and CAPE, have a crucial role in the organization, longevity and severity of deep moist convection (Weisman and Klemp, 1982, 1984). Tilting of the horizontal vorticity leads to a couplet of counter-rotating vortices (with low pressure at their centre), which induces new updraught flanks due to the vertical gradient of pressure (Rotunno, 1981). This nonlinear dynamical forcing leads the updraught to split into two cells. When the wind shear vector turns with height, one member of the vortex pair is favoured (Klemp and Wilhelmson, 1978). The longevity

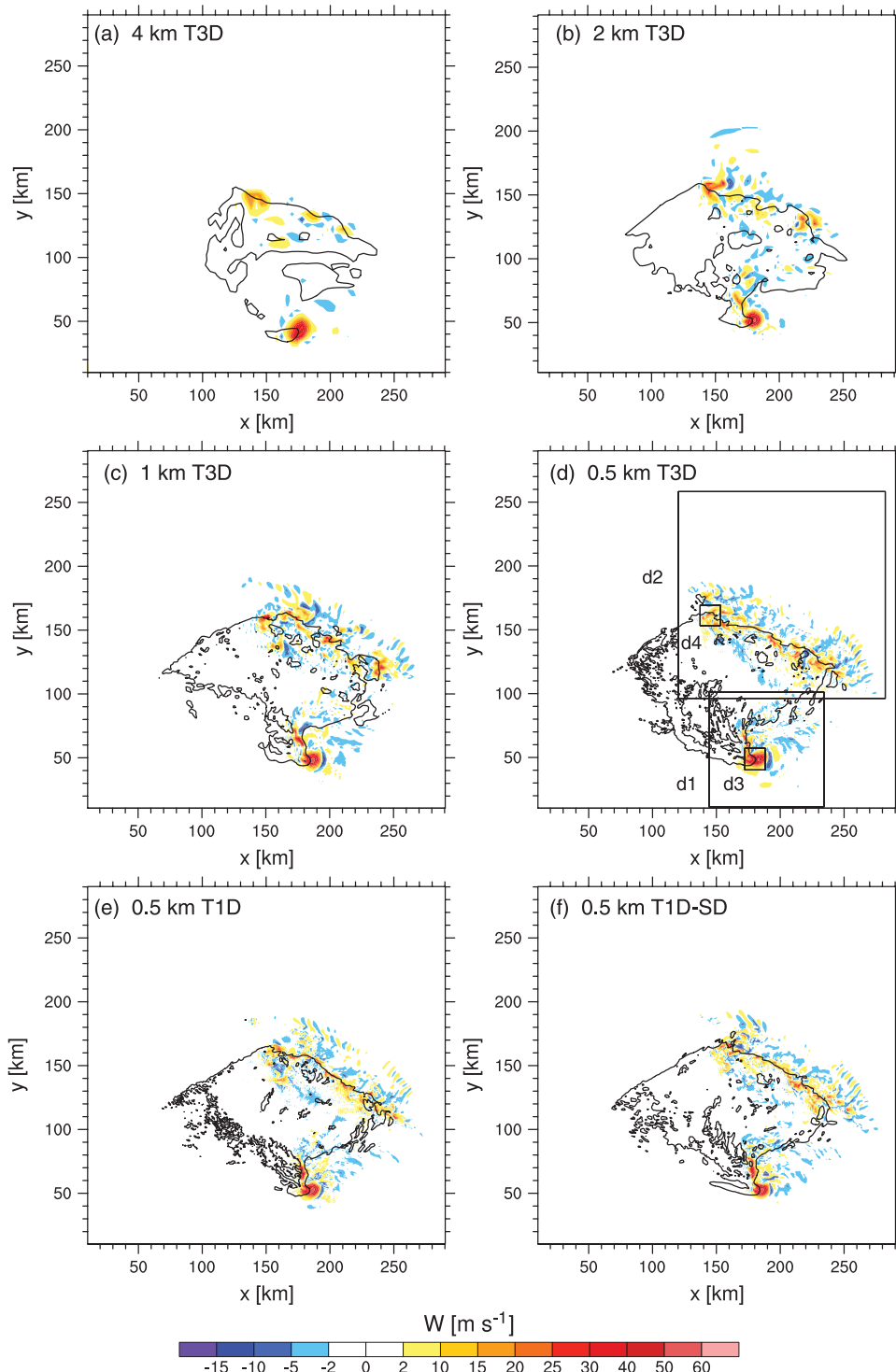


**Figure 2.** Horizontal cross-section of vertical velocities ( $\text{m s}^{-1}$ , colour shading) at 150 min and at 5 km AGL for (a) 4kmT3D, (b) 2kmT3D, (c) 1kmT3D, (d) 500mT3D, (e) 500mT1D and (f) 500mT1D-SD. The black line corresponds to  $-0.02 \text{ m s}^{-2}$  buoyancy at 500 m AGL.

and regeneration of the main updraught can be explained by a linear effect (Rotunno and Klemp, 1982): the interaction of the environmental vertical shear with the horizontal gradient of the vertical velocity of the supercell produces a dynamic vertical pressure gradient on one flank of the supercell. This dynamical forcing produces a new updraught.

If the hodograph turns clockwise with height, as in our simulations, only the right-moving system becomes a supercell. Thus, the initial cloud, generated by the rise of a warm bubble, splits into two different updraughts after 15 min. These then evolve into a right-moving supercell with a horizontal extension of about 15 km and a left-moving multicellular system composed of smaller cells (Figure 1(a)). These two systems generate precipitation (not shown) associated with cold pools (Figure 2(d)). The cyclonically rotating updraught moves to the

right of the mean wind and its trajectory is deviated to the south. The mean speed of the supercell is about  $19 \text{ m s}^{-1}$ .

Typical structures of the supercell are identifiable in Figure 1(b) and (c): the RFD located upwind of the main updraught and the FFD located below the anvil, which generate cold pools (as shown in Figure 2(d)). Cold pools are identified by the threshold of  $-0.02 \text{ m s}^{-2}$  buoyancy, the buoyancy being computed following Houze (1993) as

$$B = g \left[ \frac{\theta'}{\bar{\theta}} + 0.608q'_v + \left( \frac{R_d}{C_p} - 1 \right) \frac{P'}{\bar{P}} - q_h \right] \quad (1)$$

where  $\theta'$  is the perturbation of potential temperature from the initial mean potential temperature  $\bar{\theta}$ ,  $P'$  is the pressure perturbation from the initial mean pressure  $\bar{P}$ ,  $q'_v$  is the

perturbation of specific humidity,  $q_h$  is the sum of specific hydrometeor contents,  $R_d$  is the gas constant for dry air and  $C_p$  is the specific heat at constant pressure.

A hook echo (Stout and Huff, 1953) is also identifiable: the hydrometeors wrap around the main rotating updraught in a cyclonic motion (Figure 1(b)). Precipitating species reach the ground at the eastern side of the main updraught, whereas a bounded weak echo region (a BWER or a vault) is discernible on its western side. The vault can be well identified by following the  $2 \text{ g kg}^{-1}$  isoline of the precipitating hydrometeors mixing ratio (Figure 1(c)). The main updraught ( $W > 10 \text{ m s}^{-1}$ ) is about 18 km wide for 14 km high and reaches more than  $60 \text{ m s}^{-1}$ . The area of strong vertical velocity is associated with a mid-level mesocyclone, defined by the contour of  $0.01 \text{ s}^{-1}$  vertical vorticity in Figure 1(c). It is 7 km high and 8 km wide. Strong downdraughts are located between 8 and 16 km height on each side of the main updraught. Midlevel downdraughts, associated with evaporation and melting of hydrometeors, are also located between about 3 and 8 km.

The left-moving multicellular system seems to be a squall line, as it is composed of several convective cells forming a line with a northwest–southeast orientation. The formation of convective cells is due to a combination of several triggering mechanisms: a convergence line produced by anticyclonic mesoscale circulation associated with the left-moving initial cell, a cold pool lifting at the head of the multicell system, convergence lines of the outflows of the two systems (outflow of the multicell system and FFD outflow of the supercell) and convection initiation due to gravity waves trapped between the ground and the forward anvil (under 7000 m) (Figure 1(d)). In fact, on this last point, successive areas of positive and negative velocities with a 7 km wavelength are discernible in Figures 1(b) and 2(d) and could be the signature of trapped gravity waves, as described in Fovell *et al.* (2006) for a nocturnal squall line.

The multicellular system moves towards the northeast and becomes bigger and bigger, fed by warm moist air ahead of its leading edge. The absence of friction means that its progression does not slow (as a result of the free-slip condition at the ground). At  $t = 150$  min, the convective area is 140 km long and 50 km wide (Figure 1(b)). The vertical cross-section along the line BB' shows a succession of updraughts and downdraughts, with characteristic widths about 8–10 km smaller than those associated with the supercell, together with their intensity (Figure 1(d)).

To summarize, this simulation generated two systems with convective cells having different characteristics (size,

organization, etc.), thus allowing the impact of horizontal resolution and turbulence parametrization to be studied. Previous studies have mainly focused on describing the splitting process or the supercell characteristics, but we extend our attention here to the multicellular system, more common in real cases.

#### 4. Sensitivity to horizontal resolution

In this section, we only consider simulations with a 3D turbulence scheme. Figure 2 compares snapshots of vertical velocities at 150 min for the different resolutions. The splitting process occurs for all the simulations, generating two convective systems. It appears that the size of the multicellular system increases with increasing resolution: the length of the convective line is 90, 100, 120 and 140 km for grid spacings of 4 km, 2 km, 1 km and 500 m, respectively.

The variation is not so obvious for the supercell, as the size of the main updraught remains about 18 km, except for the 4 km grid spacing, in which it is bigger (about 25 km). This seems to indicate that the main updraught of the supercell begins to be well resolved for a grid spacing of around 2 km. At coarser resolution, the convective motions are organized on a larger scale. This is also the case for updraughts and downdraughts of the multicellular system, but the effect is noticeable for finer resolutions, as their size is smaller.

Clearly, for the 4 km simulation, the convective motions are poorly resolved, with only a few convective cells for the multicell system associated with updraughts of moderate intensity and a single updraught with too strong an intensity for the supercell. However, a test with Bechtold *et al.*'s (2001) deep convection scheme at 4 km horizontal resolution (not shown) is detrimental, as it does not succeed in structuring the two convective systems but produces light precipitation all over the domain, removing instability and underestimating total precipitation. This is in agreement with Weisman *et al.* (1997), who show that a 4 km resolution without convection parametrization allows most system-scale aspects of idealized squall line behaviour to be reproduced, or with Kain *et al.* (2008) and Weisman *et al.* (2008) for the large convective systems over the US Central Plains. A compromise would be to use a modified parametrization to greatly reduce the convective mass flux, as in Lean *et al.* (2008).

Figure 3 shows the vertical profiles of the 90th quantile (Q90) of vertical velocities (for updraught cores defined as velocities higher than a  $5 \text{ m s}^{-1}$  threshold) inside the clouds between 100 and 150 min. Two horizontal domains are considered, one

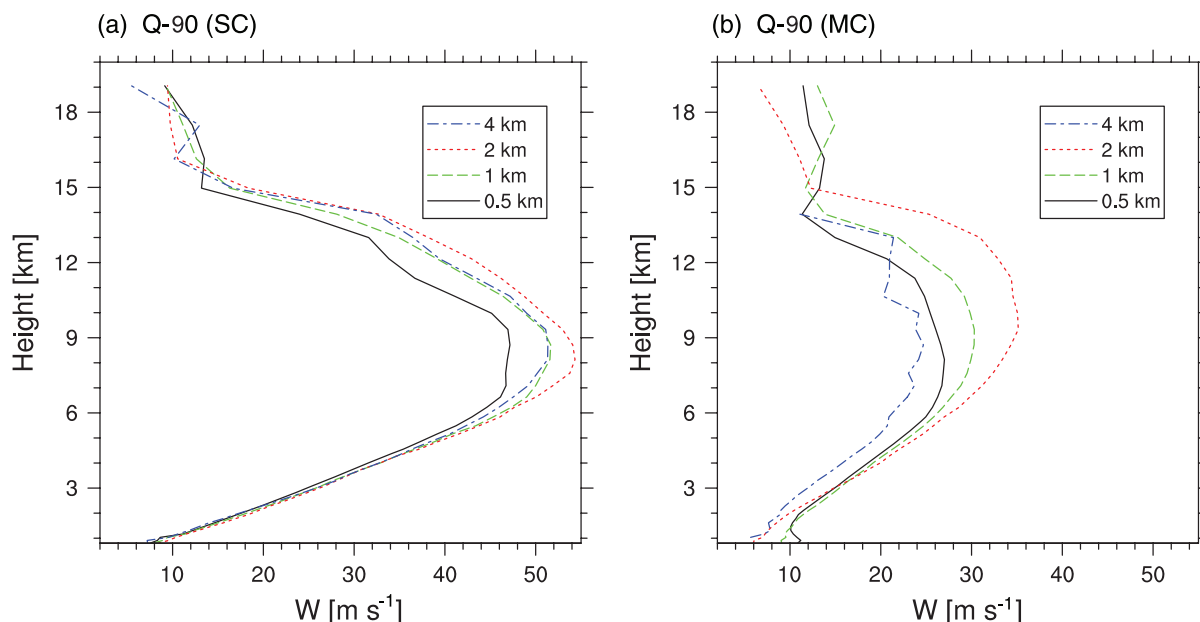
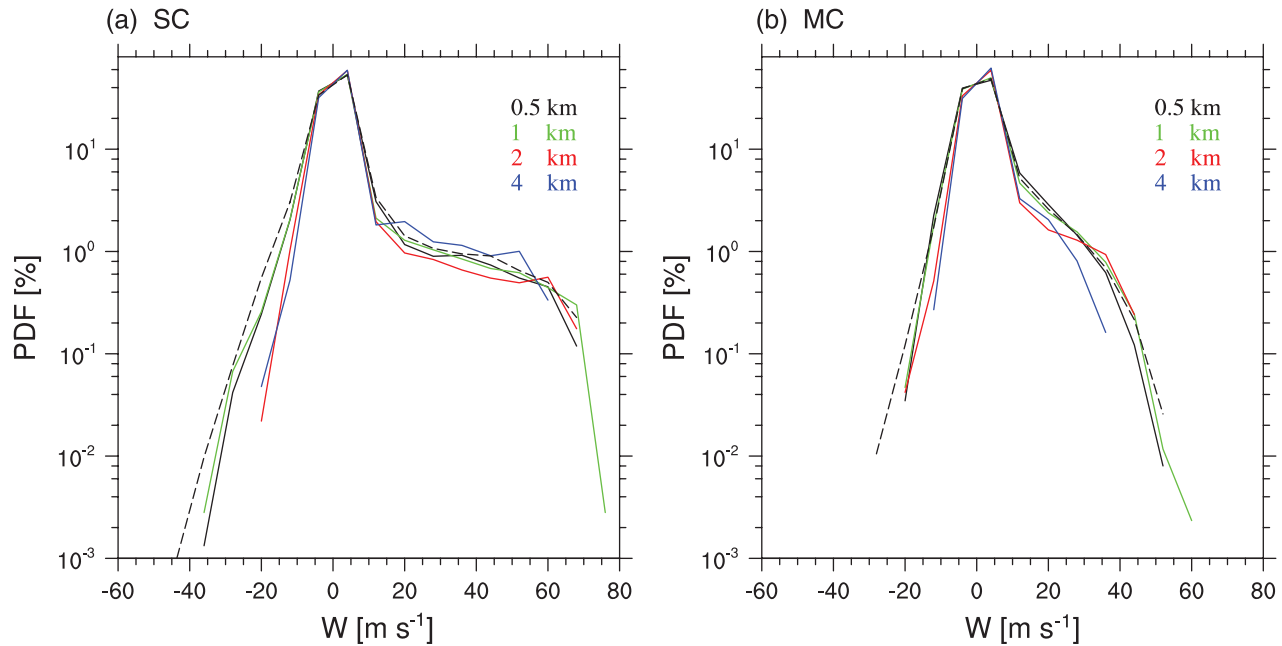


Figure 3. Vertical velocities statistics ( $\text{m s}^{-1}$ ) for the updraught cores within the clouds between 100 and 150 min for T3D runs: 90th percentile for (a) the supercell and (b) the multicellular system.



**Figure 4.** Probability density function of vertical velocities within the clouds between 100 and 150 min for 500m3D (black solid line), 500m1D (black dashed line), 1kmT3D (green line), 2kmT3D (red line) and 4kmT3D (blue line) at 8 km AGL for (a) the supercell and (b) the multicellular system.

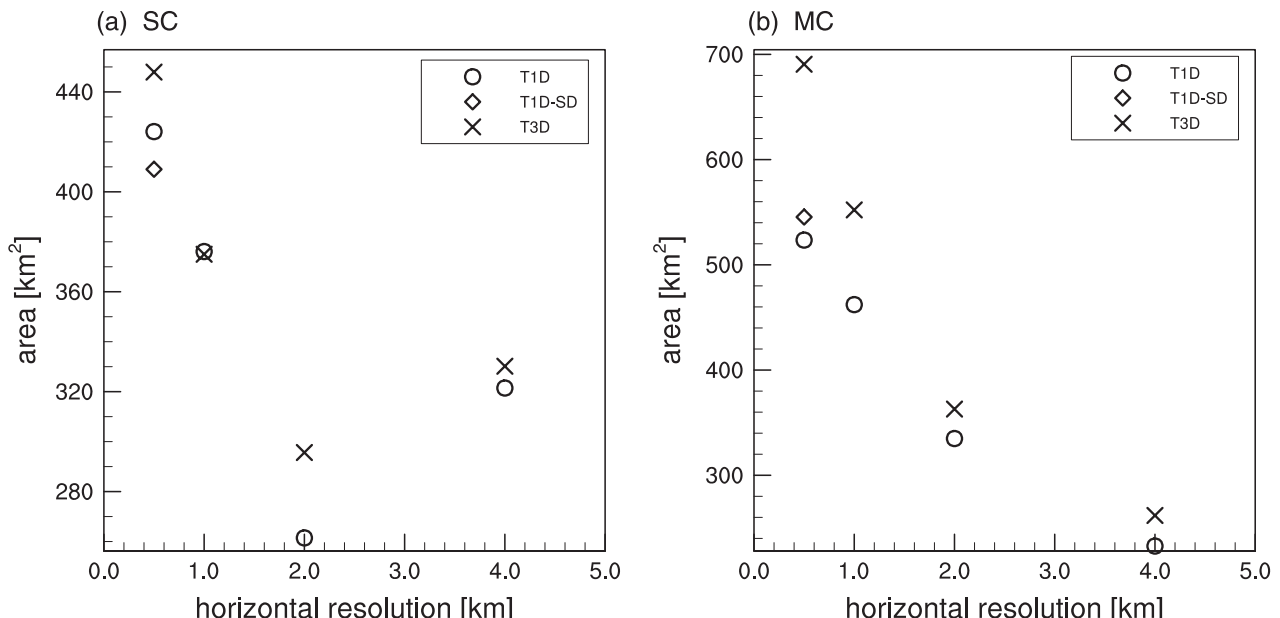
centred over the supercell (noted SC, between 16 and 100 km along the  $y$ -axis and between 12 and 292 km along the  $x$ -axis) and the other centred over the multicell system (noted MC, between 100 and 216 km along the  $y$  axis and between 12 and 292 km along the  $x$ -axis). Apart from the 4 km simulation, which shows a marginal behaviour, quantiles of the intensity of updraught cores decrease with increasing resolution (Figure 3), as does the vertical extension of updraught cores.

Figure 4 represents the probability density function (PDF) of vertical velocities. The range of velocities is wider for the supercell (between  $-35$  and  $75$   $\text{m s}^{-1}$ ) than for the multicellular system (between  $-20$  and  $60$   $\text{m s}^{-1}$ ), illustrating the fact that the supercell is associated with intense motions due to more pronounced dynamical processes. Again, the distribution of updraughts for the 4 km simulation shows that this coarse resolution does not allow the strongest updraughts to be reproduced, especially in the MC system, and increases the presence of moderate updraughts in

the SC. For the other resolutions, the highest updraughts (above about  $25$   $\text{m s}^{-1}$  for the multicell system and about  $50$   $\text{m s}^{-1}$  for the supercell) are more frequent at 2 and 1 km resolutions than at 500 m. This is coherent with the Q90 of updraught cores. In contrast, the downdraughts are less intense for the 4 and 2 km simulations compared with the 1 km and 500 m simulations, indicating that these fine structures need high resolution to be well resolved.

It should be noted that the area occupied by updraughts increases with increasing resolution (Figure 5) for both the supercell (more developed secondary updraughts) and the multicellular system (more numerous convective cells), with the exception of the 4 km resolution, which produces a very large main updraught.

Figure 6 shows the impact of horizontal resolution on accumulated precipitation and cloud cover at 8 km AGL for the whole domain. Both mid-troposphere cloud cover and accumulated precipitation amounts increase with increasing



**Figure 5.** Surface area ( $\text{km}^2$ ) covered by the updraught cores defined by a threshold of  $5$   $\text{m s}^{-1}$  at 8 km AGL time-averaged between 100 and 150 min as a function of horizontal grid spacings for (a) the supercell and (b) the multicellular system in T3D mode (black crosses), T1D mode (black circles) and T1D-SD mode (only at 500 m horizontal resolution, black diamonds).

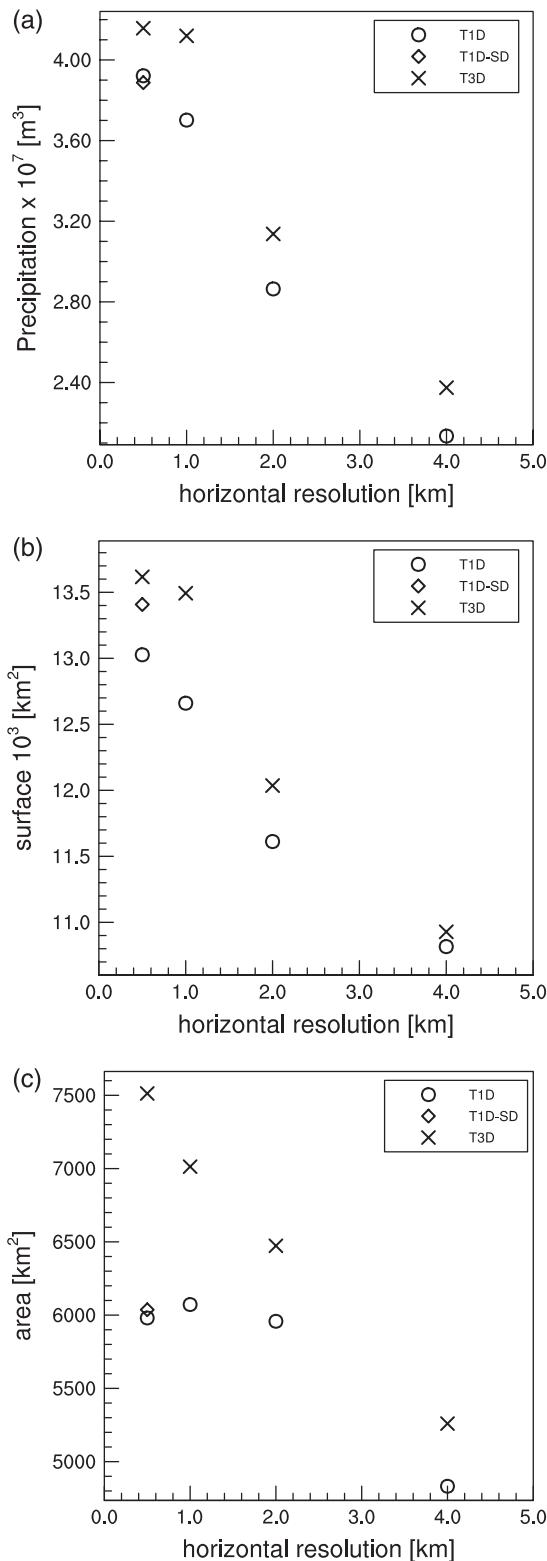


**Figure 6.** Accumulated precipitation during the first 150 min as a function of horizontal grid spacings: (a) integrated total precipitation ( $\text{m}^3$ ) and (b) surface area ( $\text{km}^2$ ) covered by the precipitation. Surface ( $\text{km}^2$ ) covered by cloud defined by a threshold mixing ratio (ice and cloud water) of  $0.001 \text{ g kg}^{-1}$  at 8 km AGL time-averaged between 100 and 150 min as a function of horizontal grid spacings (c). Diagnostics are computed for the global domain in T3D mode (black crosses), T1D mode (black circles) and T1D-SD mode (only at 500 m horizontal resolution, black diamonds).

resolution, as does the corresponding rainy area. These quantities are smaller for 4 km resolution, due to the less intense convective activity. They increase more significantly between 2 and 1 km than between 1 km and 500 m, consistent with the increase of the surface area covered by updraught cores with resolution. This also seems to be related to the horizontal extension of the leading edge of the cold pool associated with the multicellular system, which

becomes higher with increasing resolution (Figure 2). In their simulations, Bryan and Morrison (2012) showed that the accumulated precipitation decreased significantly at high resolution (250 m versus 1 km horizontal grid spacing), due to the higher rate of cloud evaporation. These differences can be explained by a strong sensitivity to the humidity of the environment, as they used a very dry initial profile in the mid-troposphere.

Concerning cold pools, Figure 7 clearly shows that the 4 km simulation generates a less intense and less extensive cold pool because of the smaller convective activity. The mean intensity of the cold pools is similar for the 2 km, 1 km and 500 m simulations. However, the mean surface area of the cold pool increases between the 2 and 1 km simulations, showing a more developed cold pool for the 1 km simulation. The differences between the 1 km and 500 m simulations are less marked. However, at the leading edge of the multicellular system, the cold pool, related to the convective activity, becomes wider when the resolution increases (Figure 2).

It should be noted that we have also assessed the impact of the time step. Decreasing the time step by a factor of 2, 4 and 8 respectively for the 2 km, 1 km and 500 m runs (i.e. keeping the same horizontal Courant number) does not change the general characteristics of either convective system (similar bulk quantities); the propagation of both systems is analogous (coinciding supercell paths, same propagation speed of the multicellular system) as well as the size of the convective structures. Even if the precipitation pattern is modified, the changes remain smaller than the changes due to the horizontal resolution (not shown).

## 5. Sensitivity to turbulence

In this section, special attention is paid to turbulence representation inside clouds on the basis of a comparison between 1D and 3D turbulence. Figure 6 shows that the area covered by ground precipitation is always smaller in T1D runs than in T3D ones, as is the high-level cloud cover and the volume of precipitation.

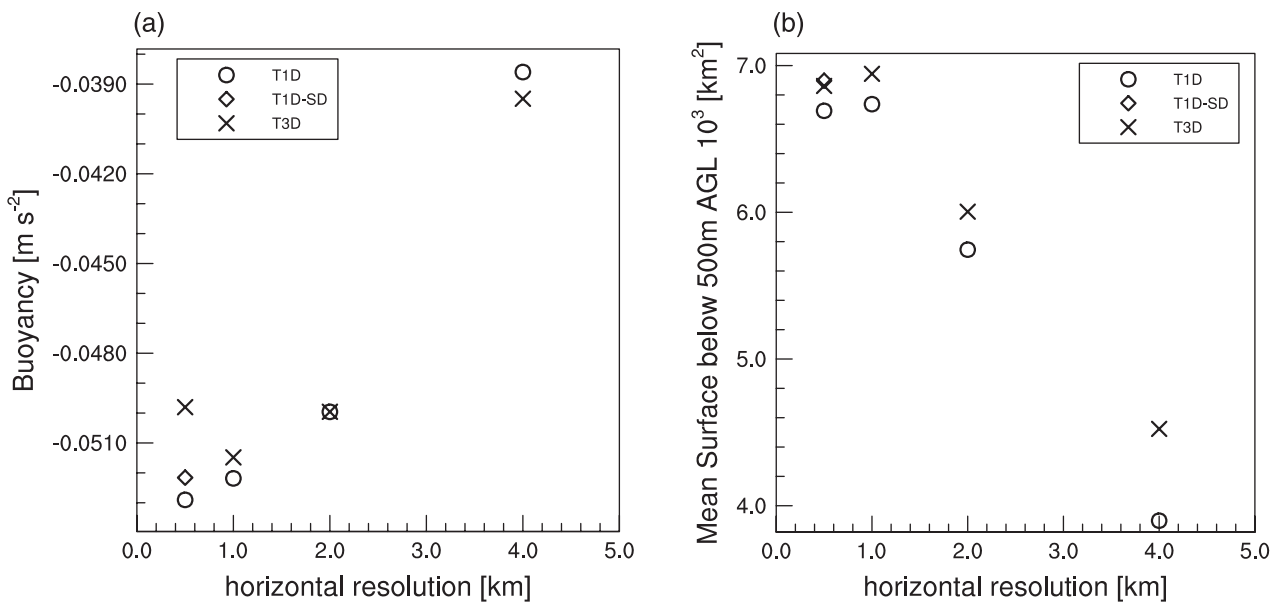
The T3D scheme induces more mixing and enhances the microphysical processes, leading to larger cloud cover in the upper levels and greater precipitation efficiency. This leads to dynamic feedback through cold pools (Figure 7(b)), also covering a slightly greater area in T3D than in T1D. The borders of the cold pool are noisy in T1D and smooth in T3D (Figure 2). It is worth noting that, in contrast, the area covered by the upper clouds is similar for 2 km, 1 km and 500 m resolution with the T1D scheme (Figure 6(c)).

As in Fiori *et al.* (2010), the maximum vertical velocity at 5 km AGL is used as a tracer to visualize the trajectories of the supercell for the 500 m horizontal grid spacing runs (500mT1D, 500mT3D and 500mNOT runs) in Figure 8. The increase of the turbulence from 500mNOT to 500mT3D increases the path curvature. There is a second signature here of the impact of the turbulence scheme on the dynamics of the convective processes.

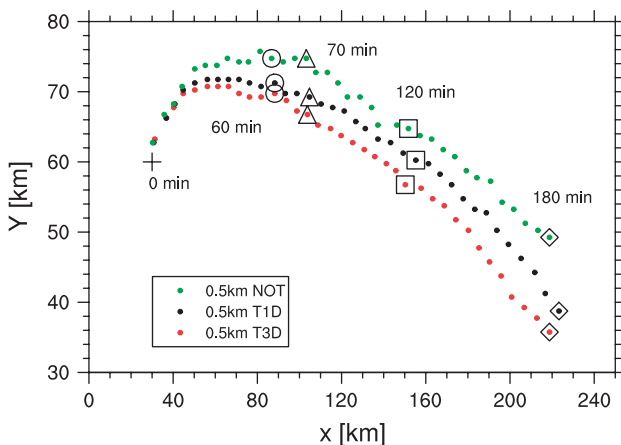
Figure 9 shows the pressure anomaly on the southeastern flank of the supercell for T3D, T1D and NOT runs. The strongest pressure anomaly in 500mT3D implies a stronger vertical gradient of the linear dynamic pressure perturbation. Thus, there is an upward vertical pressure gradient force (PGF) on the right flank of the storm that favours a more active updraught in the low levels. PGF is stronger in the 500mT3D simulation than in the others, so its trajectory is the most curved. The modification of the wind horizontal gradient magnitude may be affected by turbulent fluxes. As the gradient plays an important role in the dynamical pressure anomaly, the magnitude of this anomaly is sensitive to the turbulence parametrization.

Figure 10(a) shows the vertical profiles of the ratio between resolved and total turbulent kinetic energy, defined as

$$R = \frac{\overline{TKE_{\text{res}}}}{\overline{TKE_{\text{res}} + TKE_{\text{sgb}}}}. \quad (2)$$



**Figure 7.** Cold pool characteristics defined by a threshold buoyancy of  $-0.02 \text{ m s}^{-2}$  time-averaged between 100 and 150 min and vertically averaged between the lowest level and 500 m AGL as a function of horizontal grid spacings: (a) mean buoyancy ( $\text{m s}^{-2}$ ) and (b) surface area ( $\text{km}^2$ ) covered by the cold pool. Diagnostics are computed for the global domain in T3D mode (black crosses), T1D mode (black circles) and T1D-SD mode (only at 500 m horizontal resolution, black diamonds).



**Figure 8.** Trajectories of the supercell for 500 m horizontal grid spacing from dots indicating the successive locations of vertical velocity maxima at 5 km AGL every 5 min: no turbulence scheme (green dots), T1D mode (black dots) and T3D mode (red dots). Black circles, triangles, squares and diamonds indicate locations respectively at 60, 70, 120 and 180 min.

The resolved TKE is calculated as follows:

$$TKE_{\text{res}} = \frac{1}{2}[(U - \bar{U})^2 + (V - \bar{V})^2 + (W - \bar{W})^2], \quad (3)$$

where the overline denotes the horizontal average inside the clouds.

Surprisingly, the ratio  $R$  decreases when the horizontal resolution increases. At about 9 km AGL, the 500mT3D run has the lowest ratio (90%), whereas the 4kmT3D run has the highest (99%). This is not consistent: the resolved part of the turbulence at high resolution should be higher than at low resolution. In the same way,  $TKE_{\text{sgb}}$  increases when the horizontal resolution increases (Figure 10(b)). In other words, the production of  $TKE_{\text{sgb}}$  is higher for the 500mT3D run than for the 4kmT3D run. It is worth mentioning that the same sensitivity of this ratio to resolution is found individually for supercell or multicell systems, indicating that it is not relative to the convective organization. This deficit of physical mixing at coarse resolution also explains the excessively strong updraughts for 1km3D and 2km3D runs (Figure 3). This is in agreement with Adelman and Droege (2002), who also showed that this ratio diminishes with increasing resolution, whereas Bryan *et al.* (2003) found the opposite for the

case of a squall line. The differences possibly stem from the fact that the vertical wind shear used in our study and in Adelman and Droege (2002) is twice as strong as that used in Bryan *et al.* (2003) and the hodograph is curved (versus unidirectional shear).

With a finer horizontal resolution, small-scale structures are better represented and the resolved gradients of all variables (wind, humidity, temperature, etc.) are stronger inside the clouds. As the subgrid TKE computation is based on these gradients (directly and indirectly by the diagnostic equations for the fluxes, see Eqs (A1)–(A4)), subgrid TKE inside the clouds increases with increasing resolution (see below for the main positive contribution from dynamical production). The amount of subgrid TKE is largely underpredicted for 4 and 2 km runs, due to poorly resolved gradients. With LES simulations (with isotropic grids of a few tens of metres), the resolved percentage of TKE should approach 100% as the subgrid TKE approaches zero. Adelman and Droege (2002) found that the resolved KE increased to more than 99% with 105 m horizontal grid spacing, but only near the ground where the grid spacing was nearly isotropic.

In a similar manner, in T1D, the ratio  $R$  diminishes with increasing resolution but, as the subgrid turbulence is less (as only vertical gradients are taken into account), the ratio  $R$  is higher than in T3D runs above 6 km. The 4 km runs are again an exception, because the subgrid TKE is of the same order in T1D and T3D. This seems to suggest that the use of 1D turbulence is sufficient at 4 km horizontal grid spacing inside deep clouds but questionable at finer resolution (Figure 10).

If we focus now on 500 m horizontal resolution for the T3D run, cross-sections of the main updraught of the supercell at 150 min show the vertical structure of the horizontal wind, subgrid TKE, dynamical production and thermal production of TKE (Figure 11). The wind rolls in a swirling upward motion (Figure 11(a)). The BWER is associated with a strong northward meridional wind. Inside the updraught, diabatic heating pushes the isentropes downwards (Figure 11(b)). Above (below) the maximum heating, the vertical gradient of potential temperature is reduced (increased).

The subgrid TKE is mainly linked to dynamical processes, with high values located in the upper-level troposphere in areas with high values of potential temperature associated with downdraughts. High values tend to be located between 6 and 17 km AGL around the main updraught with a concentric structure. Low values are located on the western flank of the updraught and no subgrid TKE is present in the core of the main updraught.

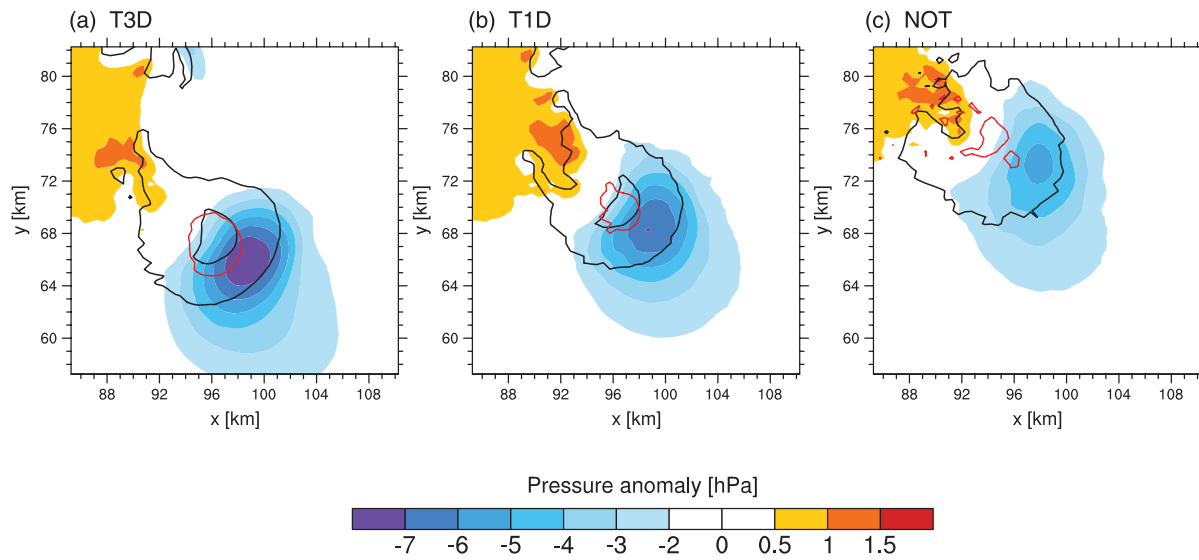


Figure 9. Horizontal cross-section of pressure anomaly (hPa, colour shading) at 70 min and at 5 km AGL for (a) 500mT3D, (b) 500mT1D and (c) 500NOT. Black (red) lines correspond to 10 and 40 m s<sup>-1</sup> (5 m s<sup>-1</sup>) vertical velocities at 5 km (0.7 km) AGL.

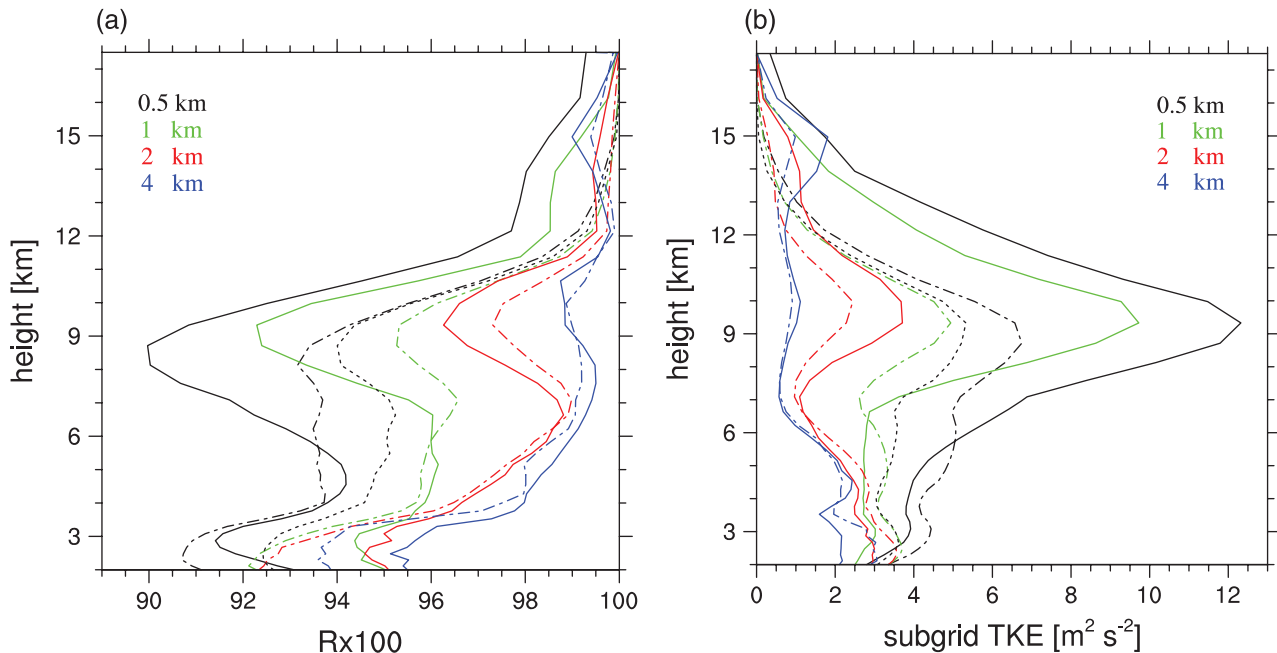


Figure 10. Vertical profiles time-averaged between 100 and 150 min and averaged over both systems for the runs in T3D mode (solid lines), T1D mode (dashed lines) and T1D-SD mode (only at 500m horizontal resolution, dotted lines): (a)  $R$  ratio between resolved TKE and total TKE and (b) subgrid TKE.

Parametrization of dynamical production of TKE is a function of resolved horizontal and vertical wind shear. Dynamical production is mainly positive and located in areas of strong gradients of velocities, consistent with the expression of momentum flux (see Eq. (A2)). The predominance of dynamical production is also confirmed for both systems in Figure 12, with a peak at 9 km AGL. Thermal production is mainly negative, with strong values in areas of strong positive vertical gradient of  $\theta_l$  (associated with strong downdraughts). Thermal production is positive only when the vertical gradient of  $\theta_l$  is negative, as the vertical flux term of  $\theta_l$  is dominant in the flux of virtual temperature in comparison with the vertical flux term of  $r_{np}$  (see Eqs (A3) and (A5)).

Thermal production is near-zero in the main updraught of the supercell, as the vertical gradients of  $r_{np}$  and  $\theta_l$  are very weak (Figure 11(c) and (d)). The dynamical production is also very weak in the main updraught, as the six fluxes of momentum are very weak (not shown). It is worth noting that there is a little more  $TKE_{sbg}$  inside the updraughts of the multicellular system (about 30–35 m<sup>2</sup> s<sup>-2</sup> instead of 10–15 m<sup>2</sup> s<sup>-2</sup>), but the peak remains around 9 km AGL.

The lack of turbulence is quite surprising. Various reasons for this can be hypothesized. Some numerical and observational studies have suggested that turbulence is inhibited inside the main updraught of supercells, due to high helicity (Lilly, 1986; Krauss and Marwitz, 1984). Another hypothesis is that the residence time of a transient disturbance may not be long enough for instabilities to grow to significant amplitude, as air parcels are quickly advected inside the strong updraught of the supercell; this assumption is based on a distinction between local and global instabilities (Pierrehumbert, 1984). Another reason may be that a large part of the turbulence could be resolved due to the large structure of this updraught. Finally, this may also reflect a limitation of the turbulence scheme, as the turbulent fluxes are parametrized with an eddy viscosity/diffusivity term (see Eqs. (A2)–(A4)) that vanishes when gradients are zero. A more sophisticated parametrization using additional terms, as in Moeng *et al.* (2010), could be more appropriate.

Small subgrid TKE is simulated at the cloud boundary, meaning that entrainment of dry air at the interface between the cloud and the environment is insufficiently represented by the turbulence parametrization at 500 m horizontal resolution.

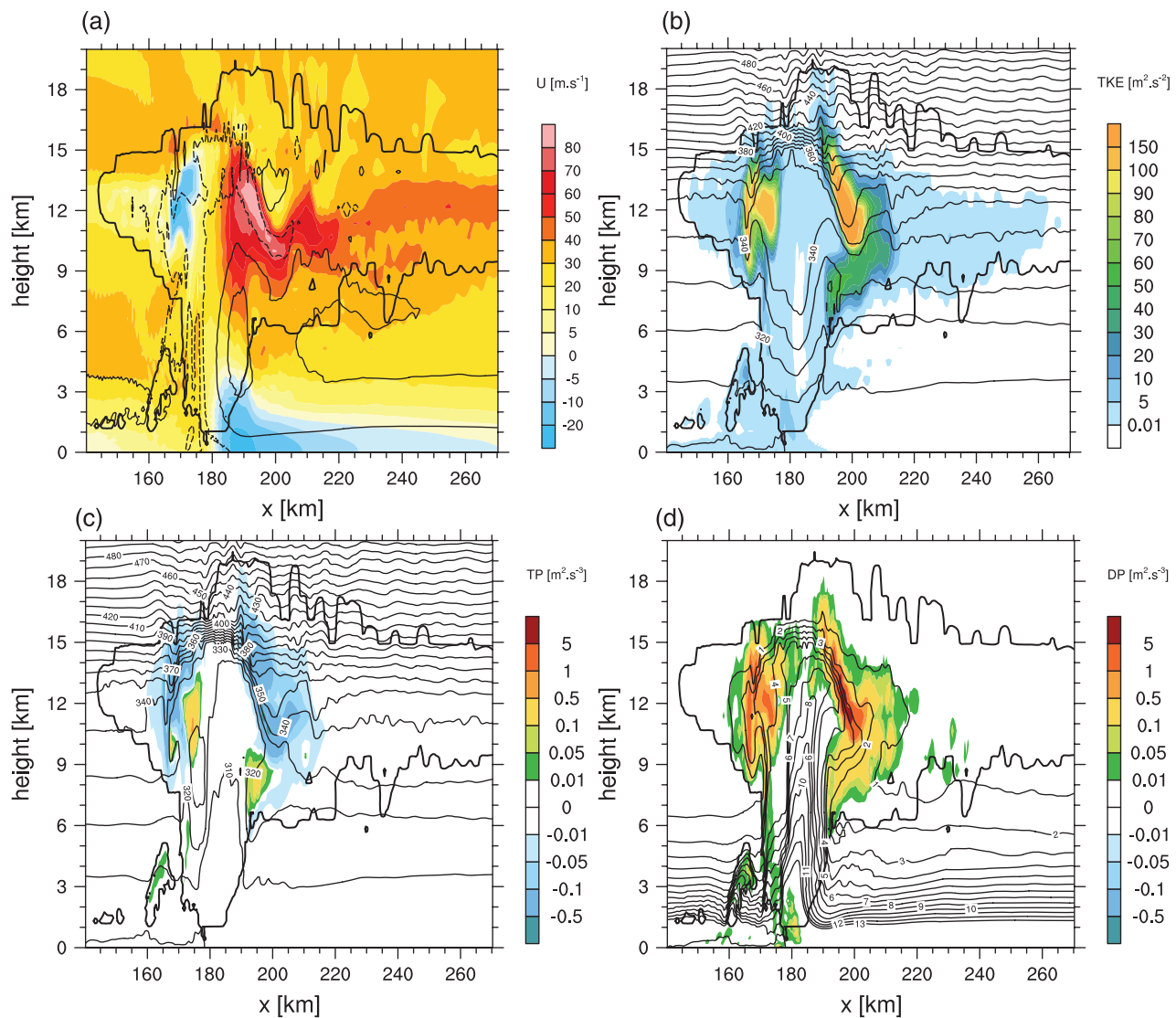


**Figure 11.** Vertical cross-sections along AA' line indicated in Figure 1(b) through the supercell at 150 min: (a)  $U$  wind component ( $\text{m s}^{-1}$ , colour shading),  $V$  wind component ( $10, 30 \text{ m s}^{-1}$ , thin light grey solid line and  $-10 \text{ m s}^{-1}$ , thin light grey dotted line) and vertical velocities ( $10 \text{ m s}^{-1}$ , heavy grey line), (b) subgrid TKE ( $\text{m}^2 \text{ s}^{-2}$ , colour shading) and potential temperature (K, black lines), (c) thermal production of TKE ( $\text{m}^2 \text{ s}^{-3}$ , colour shading) and liquid potential temperature (K, black lines) and (d) dynamical production of TKE ( $\text{m}^2 \text{ s}^{-3}$ , colour shading) and total non-precipitating mixing ratio ( $\text{g kg}^{-1}$ , black lines).

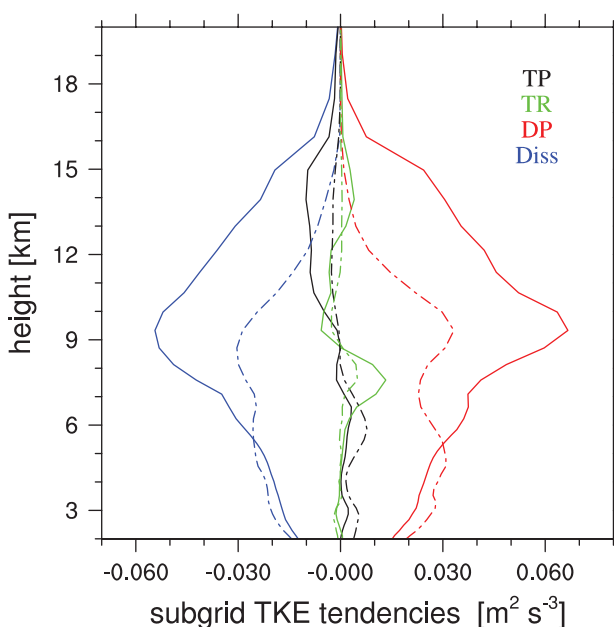


**Figure 12.** Vertical profiles of TKE tendencies ( $\text{m}^2 \text{ s}^{-3}$ ) for 500mT3D (solid lines) and 500mT1D (dashed lines) runs time-averaged between 100 and 150 min and averaged over both systems: thermal production (black line), dynamical production (red line), dissipation (blue line) and transport (green line).

Taking account of the horizontal gradients with the 3D turbulence scheme results in more subgrid TKE (Figure 10(b)) for the T3D scheme with enhanced thermal and dynamical production terms (Figure 12). This also has an impact on vertical motions, with reduced intensity for updraughts and downdraughts when a T3D scheme is used (Figure 4). The dominant contribution of the dynamics to the production of TKE also explains why, at low resolution, the gradients are so poorly resolved that a deficit of production of TKE ensues, showing the limits of the parametrization inside the clouds.

Figure 13(a) and (b) shows the spatial structure of subgrid TKE inside the supercell for the 500mT3D and 500mT1D runs (at 10 km AGL). In T3D runs, the field is smoother than in T1D runs, because physical mixing occurs in the horizontal direction, contrary to what happens in T1D runs. This is confirmed by the vertical velocity spectra in Figure 14. At first glance, the two convective systems have different spectra. The magnitude of the variances cannot be directly compared between the two sets of spectra, because the computation domain is different, but the shape of the spectra is informative. The supercell spectrum peaks between 30 and 20 km wavelength, as in Fiori *et al.* (2010), whereas the peak of variance is between 20 and 15 km for the multicell system, due to the fact that vertical motions are larger in the supercell. The inertial subrange, defined by the spacing of the spectrum from the  $-5/3$  theoretical slope, is also more

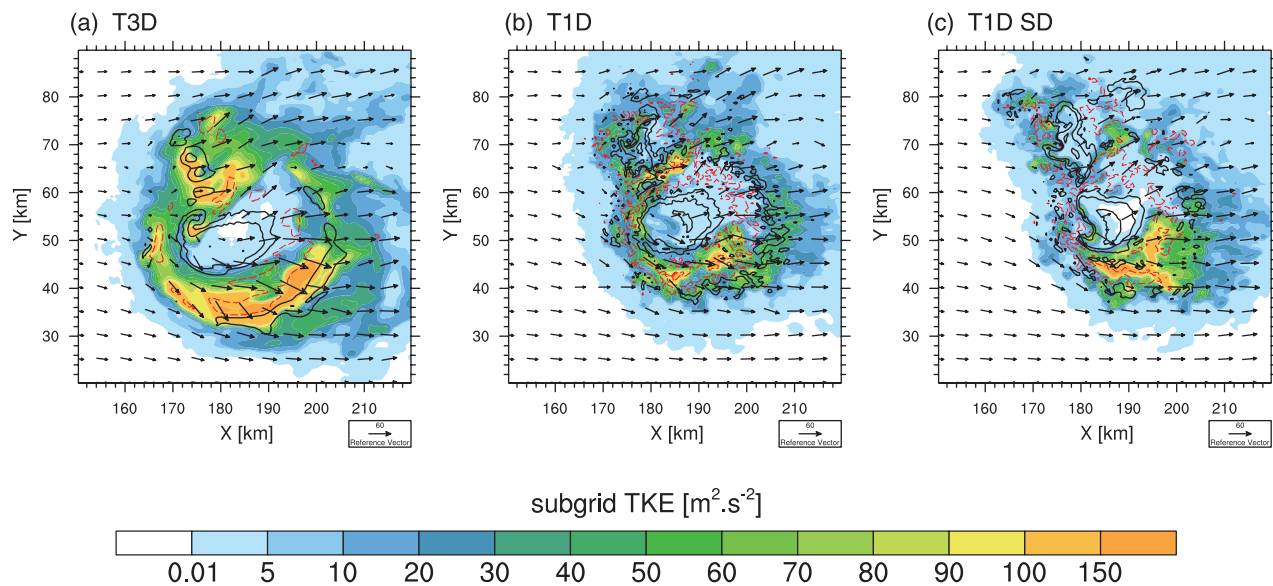


**Figure 13.** Horizontal cross-sections at 10 km AGL and 150 min over the supercell: subgrid TKE ( $\text{m}^2 \text{s}^{-2}$ , colour shading), black lines correspond to vertical velocity ( $10, 40, 60 \text{ m s}^{-1}$ ) and black arrows correspond to horizontal wind ( $\text{m s}^{-1}$ ) for (a) 500mT3D run, (b) 500mT1D run and (c) 500mT1D-SD run.

extensive for the supercell (between about 10 and 4 km) than for the multicellular system (between about 7 and 4 km).

For both systems, we can first note that the effective resolution is between 3 and 4 km, corresponding to  $6-8\Delta x$ . Moreover, there is more dissipative effect at small scales for the 500mT3D run than for the 500mT1D run, in agreement with Figure 13. In T1D, the spectral tail is too high at the smallest scales, meaning that the turbulent dissipation is too low. Moreover, there is a slight deficit of variance at larger scales in 1D compared with 3D for the multicell system, indicating that the 3D turbulence scheme leads to motions organized at a larger scale in order to compensate for dissipation at the smallest scales. These two effects of accumulation of energy at the tail and large loss of variance at larger scales in T1D are enhanced when no turbulence scheme is used (500mNOT).

In order for comparison with the results of Fiori *et al.* (2010), who surprisingly, found more dissipation with 1D turbulence than 3D but with some additional diffusion added only in 1D, the 500mT1D-SD run (strong numerical diffusion with 1D turbulence) was compared with 500mT1D and 500mT3D. The value of the damping coefficient was chosen to obtain the same diffusion at  $2\Delta x$  wavelength in 500mT1D-SD and 500mT3D between 3 and 9 km (Figure 14(a)).

With 500mT1D-SD, the diffusion is logically enhanced compared with the 500mT1D run but still differs from 500mT3D. The smoothing is illustrated in Figure 2, where the borders of the cold pool seem similar in 500mT1D-SD and 500mT3D and differ from 500mT1D; this is also confirmed by similar surface areas covered by the cold pool in Figure 7(b). However, the surface covered by the updraught cores in both supercell and multicells is approximately the same in 500mT1D-SD as in 500mT1D (Figure 5), as are the volume of precipitation (Figure 6(a)) and the cold pool intensity (Figure 7(a)). Only the precipitation area is intermediate between 1D and 3D (Figure 6(b)). This is also illustrated in the supercell (Figure 13(c)), where the vertical velocities at 10 km height are smoother than for the 500mT1D run but the size of the concentric structure remains smaller than for the 500mT3D run, with a more intense updraught core. Moreover, subgrid TKE is considerably smaller than in 500mT3D but also smaller than in 500mT1D, as demonstrated in Figure 10. The damping from the strong numerical diffusion smoothes the gradients and therefore reduces the physical mixing produced by the turbulence scheme.

As the damping at the spectral tail in 500mT1D-SD was defined as equivalent to that in the 500mT3D run between 3 and 9 km height, there is no excess of energy in 500mT1D-SD

as in 500mT1D for the smallest scales. However, the variance is lower for larger scales (above 20 km for the supercell and above 5–7 km for the multicell) compared with the 500mT3D run. Moreover, the dissipation at the spectral tail is still more pronounced between 9 and 12 km for the 500mT3D run, as higher subgrid TKE enhances the mixing. This more efficient mixing is based on physical aspects and located in areas of strong gradients. As argued, for example, by Weisman *et al.* (1997) and Takemi and Rotunno (2003), the primary goal of computational smoothing is to maintain numerical stability of the solution by reducing spurious oscillation but with minimal impact on physically important scales. Our belief is that it clearly should not be used to replace physical mixing, which must be handled preferentially by a turbulence scheme.

Spectra are also computed when focusing on the main updraught of the supercell with a  $10 \times 10 \text{ km}^2$  domain (Figure 14(e)). The slope of the spectra is less than  $-5/3$ , suggesting that the cascade of energy from large to small scales is inhibited, but not removed, inside the main updraught area. This is in agreement with the study of Lilly (1986), who speculated that storms characterized by high helicity were less prone to dissipation, thus explaining the greater longevity of these storms. In contrast, it is worth noting that an inertial subrange is clearly discernible when focusing on the multicellular system (Figure 14(f)) or on the stratiform part of the supercell (not shown).

## 6. Conclusion

In this study, idealized simulations of deep moist convection have been performed to assess sensitivity to the horizontal resolution (ranging from 4 km for the lowest resolution to 500 m for the highest) and the turbulence scheme (T1D mode versus T3D mode). Classically, for all simulations, the initial cell splits into two convective systems: a leftward-moving multicellular system and a rightward-moving supercell. The supercell produces the most intense motions, due to enhanced dynamical processes. The multicellular system generates the largest system, as it is organized in a line composed of convective cells of smaller size.

Obviously, the convective motions are poorly resolved for the 4 km simulation, where the single updraught is too intense in the supercell and there are few cells in the multicellular system. It is shown that this horizontal resolution is in the grey zone for convection, as the use of a deep convection scheme leads to poor structure in the convection. For the other simulations, the 90th quantile of the intensity of updraught cores decreases with increasing resolution. This suggests a lack of entrainment

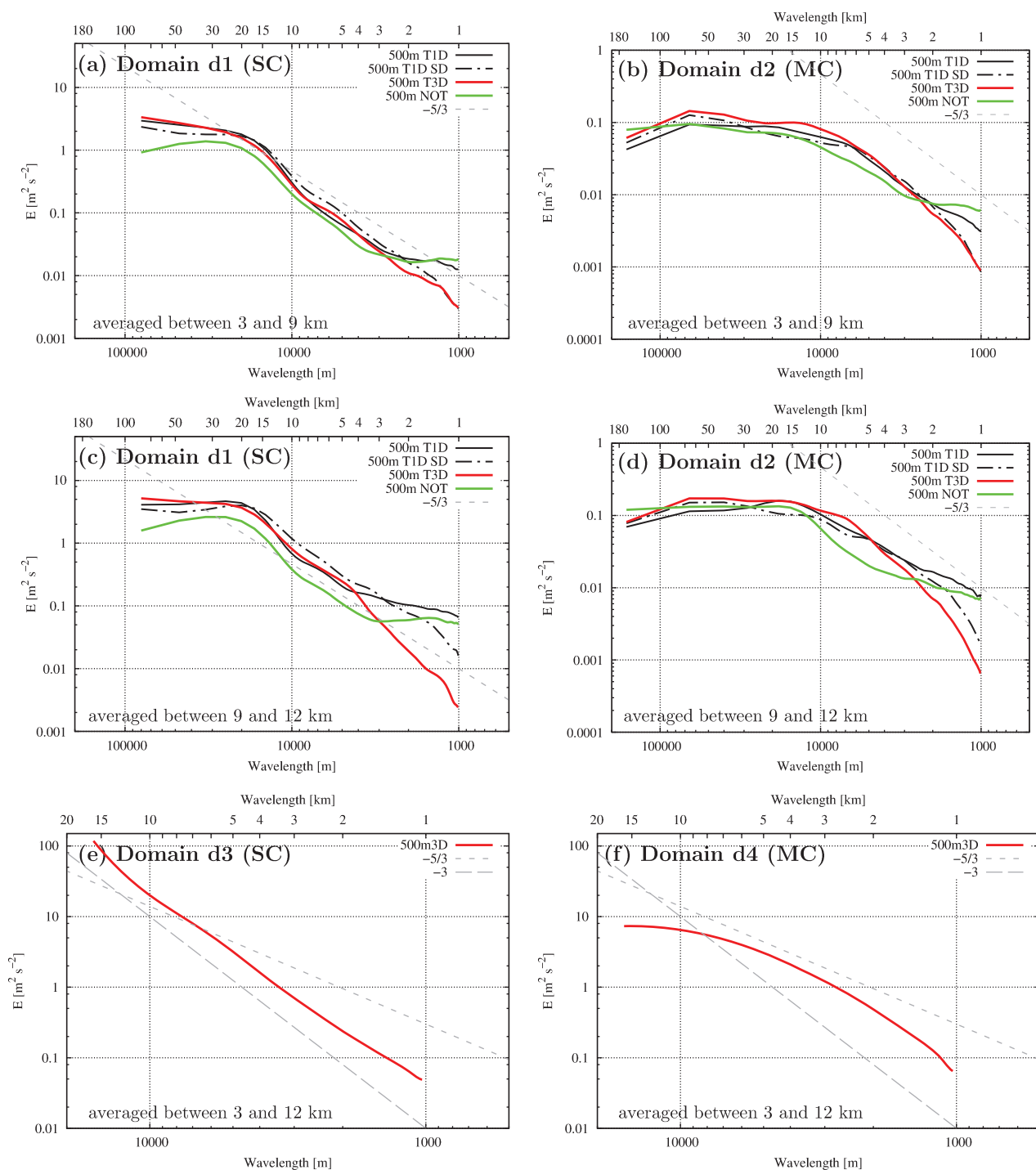


**Figure 14.** Vertical velocity spectra averaged between (a, b) 3 and 9 km, (c, d) 9 and 12 km and (e, f) 3 and 12 km at 150 min for 500mNOT, 500mT1D, 500mT3D and 500mT1D-SD runs for subdomains centred over (a, c) the supercell and (b, d) the multicellular system. Enlargements are shown for (e) the supercell updraught and (f) a convective part of the multicellular system. The short-dashed (long-dashed) line corresponds to  $-5/3$  ( $-3$ ) slope, illustrating the  $k^{-5/3}$  ( $k^{-3}$ ) regime at the mesoscale (at large scales). Subdomains are indicated by the boxes in Figure 2(d).

that produces excessively strong updraughts, mainly at coarse resolution.

The accumulated precipitation amount and surface area increase with higher resolution, in association with the increase of the area covered by the updraughts. The size of the leading edge of the multicellular system also increases, as does the cloud cover.

Several of these findings from horizontal resolution experiments have practical application to weather prediction. In terms of occurrence of convective systems, the four resolutions manage to generate two convective systems with a splitting process. Even at 4 km horizontal grid spacing, the supercell structure is identifiable, giving information in terms of severity of deep convection and potential danger. This may be related to the work of Kain *et al.* (2008), who found that 4 km horizontal grid

spacing was sufficient to represent mesoscale convective systems of large storms developing over the plains of the central United States, such as squall lines, bow echoes and supercells, at lower computational cost than 2 km resolution. They found that there were systematic differences between 2 and 4 km forecasts (analyzed 18–30 h after model initialization), with 2 km resolution giving more detailed structure and more numerous small-scale features but adding little practical value for forecast guidance. However, in our study the multicell system is only crudely represented at 4 km, in accordance with numerous other studies (e.g. Lean *et al.*, 2008) that have shown that convection is under-resolved at 4 km. Overall, the differences between the 2 and 1 km simulations are more pronounced than those between the 1 km and 500 m simulations, suggesting a beginning of convergence for the mean physical characteristics of the simulated convective

systems, e.g. intensity and area of the cold pools. A significant gap between simulations with 2.5 and 1 km grid spacings was also found in Ricard *et al.* (2013) for a real case of isolated convection with the same Meso-NH model (and thus with the same effective resolution). Moreover, the convective system as a whole exhibits stronger downdraughts for 500 m and 1 km simulations and also higher amounts of precipitation (30% more). These significant differences can give precious indications about the potential severity of storms, in particular in terms of wind damage and flooding. The differences between 500 m and 1 km are less marked and add little value as forecast guidance. Therefore, our recommendation would be to use horizontal resolution of the order of 1 km to forecast deep convection. This is already the case at the Met Office, as UM runs at 1.5 km grid spacing. In the same way, at Meteo-France, the horizontal resolution of the operational fine-scale model AROME will be improved from 2.5 to 1.3 km in 2014. Preliminary tests with the AROME model using a 1.3 km horizontal resolution have shown that the size and intensity of convective cells are closer to precipitation structures observed by radar (Seity *et al.*, 2014). Of course, it should be noted that a limitation of the present study is that an idealized framework is used with no representation of a surface layer, radiation, orography or Coriolis force with very short lead time. Moreover, as this study focuses on organized deep convection in a sheared environment, conclusions are not necessarily applicable to all convective phenomena (in particular to shallow convection). Generalization to other systems would need further studies.

From an operational point of view, it should be mentioned that there are other ways to improve forecast than increasing resolution, such as improving the data assimilation, improving physical parametrizations or choosing a probabilistic system instead of a deterministic one. For the same computational cost, rather than using a deterministic simulation with high resolution, it may be wise to consider a small ensemble with coarser resolution members or to enlarge the forecast domain. In the same vein, more efficient dynamical schemes (for example a semi-implicit semi-Lagrangian scheme versus an explicit Eulerian scheme) can also be considered to improve the computational time. In practice, it appears that all these approaches are complementary and that the increase in computational resources of many weather forecast centres is accompanied at the same time by an increase in resolution, an enlargement of the size of the forecast domain and the operational implementation of probabilistic systems at convective scales.

Concerning sensitivity to the turbulence scheme, the T3D runs induce more mixing and enhance the microphysical processes, producing larger amounts of cloud cover and precipitation. The T3D scheme also induces a stronger mid-level pressure anomaly on the southeastern flank of the supercell, enhancing the vertical pressure gradient and the regeneration of the main updraught on the right flank of the supercell. This consequently accentuates the curvature of its trajectory towards the south, strengthening the linear dynamical forcing. Also, taking the horizontal gradients into account with the 3D turbulence scheme results in more subgrid TKE, with reduced intensity for updraughts and downdraughts.

Moreover, the dissipative effect is insufficient at small scales for the 500mT1D run compared with 500mT3D, as energy builds up to physically unrealistic levels at the highest wavenumbers (Skamarock, 2004). There is also a large loss of variance at larger scales. These two biases are more pronounced without a turbulence scheme, leading to the conclusion that T1D does not produce enough mixing effects.

Increasing numerical diffusion to compensate for the insufficient mixing in 1D improves the finest scales by smoothing and removing the excess of variance, but maintains the deficit of variance at larger scales and also decreases the physical mixing by smoothing the gradients. The use of artificial numerical filters, stronger than the minimum value necessary to damp the  $2\Delta x$  waves, should therefore be avoided as it cannot replace physical mixing based on turbulence-closure schemes.

The ratio between resolved and total TKE decreases with increasing horizontal resolution, which is not satisfactory: the proportion of turbulence resolved at high resolution should be higher than that at low resolution. At coarse resolution, the gradients are so poorly resolved that this leads to a deficit in production of TKE, showing the limits of the parametrization inside the clouds. This deficit of physical mixing at coarse resolution also explains why updraughts are too strong in 1 and 2 km simulations. Also, the subgrid TKE is of the same order in T1D and T3D runs at 4 km horizontal grid spacing, suggesting that the use of 1D versus 3D turbulence is sufficient (even if not satisfactory) at this resolution inside deep clouds. However, this is no longer true at finer resolution, as the differences between the two schemes become larger. This suggests that a 3D turbulence scheme may be necessary for deep convection clouds from 2 km horizontal grid spacing. This is a major point for current kilometric NWP models, most of which use a 1D turbulence scheme.

The 3D turbulence inside convective clouds has also been explored in detail at 500 m horizontal grid spacing. The subgrid TKE is mainly produced by dynamical processes and located in areas of strong gradients of velocities, whereas thermal production is mostly negative. Small subgrid TKE is simulated at cloud boundaries, suggesting that entrainment of dry air at the interface between the cloud and the environment is not sufficiently represented by the turbulence parametrization even at 500 m horizontal resolution.

Inside the main updraught of the supercell, there is no subgrid TKE with near-zero thermal and dynamical production, which seems more acceptable as most of the turbulence may be resolved. Moreover, spectral analysis of vertical velocities indicates that the cascade of energy is inhibited within the main rotating updraught, due to high helicity. It also illustrates that the inertial subrange is larger for the supercell than for the multicellular system, with a peak of variance shifted to smaller scales for the latter.

Further studies are needed to address the deficiencies of the turbulence scheme inside deep clouds by focusing on intermediate scales. In particular, LES simulations on deep convection are needed to provide a reference of intracloud turbulence features. Using idealized simulations of squall lines, Bryan *et al.* (2003) have shown that a grid spacing of  $\mathcal{O}(100 \text{ m})$  is required for traditional LES closures. Thus, we plan to run the Meso-NH model at 50 m horizontal resolution for a single deep convective cell to obtain a benchmark simulation. Then simulations will be conducted at coarser resolutions. The structure of turbulence at lower resolution will be compared with the benchmark run in order to improve the turbulence scheme, when the eddies are partly or fully subgrid.

## Appendix A: The turbulence scheme in the Meso-NH model

The second-order moment equations are separated into isotropic and anisotropic parts for the Reynolds tensor. The representation of the isotropic part is based on a prognostic equation for the turbulent kinetic energy (TKE) given in Eq. (A1), used with conservative variables for moist non-precipitating processes, combined with a diagnostic mixing length representing the size of the most energetic eddies:

$$\begin{aligned} \frac{\partial e}{\partial t} = & -\frac{1}{\rho_{\text{dref}}} \frac{\partial(\rho_{\text{dref}} \bar{e} \bar{u}_i)}{\partial x_j} - \bar{u}'_i \bar{u}'_j \frac{\partial \bar{u}_i}{\partial x_j} + \frac{g}{\theta_{\text{vref}}} \bar{u}'_3 \theta'_v \\ & + \frac{1}{\rho_{\text{dref}}} \frac{\partial}{\partial x_j} (C_{2m} \rho_{\text{dref}} L e^{1/2} \frac{\partial e}{\partial x_j}) - C_\epsilon \frac{e^{3/2}}{L}, \quad (\text{A1}) \end{aligned}$$

where  $e$  is the TKE that evolves respectively from advection (first term on the right-hand side), dynamical production (second term), thermal production (third term), turbulent transport (fourth term) and dissipation (fifth term).  $u_i$  represents the  $i$ th component of the velocities,  $\theta_v$  is the virtual temperature,  $\rho_{\text{dref}}$  and  $\theta_{\text{vref}}$  are the reference density and virtual temperature

profiles respectively,  $g$  is the acceleration due to gravity,  $L$  is the mixing length and  $C_{2m}$  and  $C_\epsilon$  are closure constants. Bars denote means, while primes denote turbulent components.

For all other quantities, such as fluxes and the anisotropic part of the Reynolds tensor, the equations are simplified (stationarization for the anisotropic part, third-order moments are neglected, etc.: see Redelsperger and Sommeria (1981) for more details). This leads to the following diagnostic equations for the fluxes:

$$\overline{u'_i u'_j} = \frac{2}{3} \delta_{ij} e - \frac{4}{15} \frac{L}{C_m} e^{1/2} \left( \frac{\partial \overline{u_i}}{\partial x_j} + \frac{\partial \overline{u_j}}{\partial x_i} - \frac{2}{3} \delta_{ij} \frac{\partial \overline{u_m}}{\partial x_m} \right), \quad (A2)$$

$$\overline{u'_i \theta'_l} = -\frac{2}{3} \frac{L}{C_s} e^{1/2} \frac{\partial \overline{\theta_l}}{\partial x_i} \phi_i, \quad (A3)$$

$$\overline{u'_i r'_{np}} = -\frac{2}{3} \frac{L}{C_h} e^{1/2} \frac{\partial \overline{r_{np}}}{\partial x_i} \psi_i, \quad (A4)$$

where  $\theta_l$  is the liquid potential temperature,  $r_{np}$  is the total non-precipitating total water mixing ratio (sum of water vapour, cloud water and ice),  $\delta_{ij}$  is the Kronecker delta tensor,  $\psi_i$  and  $\phi_i$  are stability functions defined in Cuxart *et al.* (2000), the Einstein summation convention applies for subscripts  $m$  and  $C_s, C_h, C_m$  are constant from pressure-correlation parametrization.

The flux of virtual temperature, needed for the TKE equation, can be obtained by

$$\overline{u'_3 \theta'_l} = E_\theta \overline{u'_3 \theta'_l} + E_{\text{moist}} \overline{u'_3 r'_{np}}, \quad (A5)$$

where  $E_\theta$  and  $E_{\text{moist}}$  are coefficients described in Redelsperger and Sommeria (1986).

## Appendix B: The BL89 mixing length

The mixing length  $L$  is defined as follows:

$$L = \left[ \frac{(l_{\text{up}})^{-2/3} + (l_{\text{down}})^{-2/3}}{2} \right]^{-3/2}, \quad (B1)$$

with the distances  $l_{\text{up}}$  and  $l_{\text{down}}$  as follows:

$$\begin{aligned} \int_z^{z+l_{\text{up}}} \frac{g}{\theta_{\text{vref}}} [\theta_{\text{v}}(z') - \theta_{\text{v}}(z)] dz' &= e(z), \\ \int_{z-l_{\text{down}}}^z \frac{g}{\theta_{\text{vref}}} [\theta_{\text{v}}(z) - \theta_{\text{v}}(z')] dz' &= e(z), \\ l_{\text{down}} &\leq z. \end{aligned} \quad (B2)$$

## Acknowledgements

The authors acknowledge the two anonymous reviewers, whose comments and suggestions helped to improve the original manuscript significantly. We also thank Jean-Philippe Lafore, Valery Masson, and Jeffrey Beck for helpful discussions.

## References

- Adlerman EJ, Droegeemeier KK. 2002. The sensitivity of numerically simulated cyclic mesocyclogenesis to variations in model physical and computational parameters. *Mon. Weather Rev.* **130**: 2671–2691.
- Baldauf M, Seifert A, Förstner J, Majewski D, Raschendorfer M, Reinhardt T. 2011. Operational convective-scale numerical weather prediction with the COSMO model: Description and sensitivities. *Mon. Weather Rev.* **139**: 3887–3905.
- Bechtold P, Bazile E, Guichard F, Mascart P, Richard E. 2001. A mass-flux convection scheme for regional and global models. *Q. J. R. Meteorol. Soc.* **127**: 869–886.
- Bougeault P. 1982. Cloud-ensemble relations based on the gamma probability distribution for the higher-order moments of the planetary boundary layer. *J. Atmos. Sci.* **39**: 2691–2700.
- Bougeault P, Lacarrere P. 1989. Parameterization of orography-induced turbulence in a mesobeta-scale model. *Mon. Weather Rev.* **117**: 1872–1890.
- Bryan GH, Morrison H. 2012. Sensitivity of a simulated squall line to horizontal resolution and parametrization of microphysics. *Mon. Weather Rev.* **140**: 202–225.
- Bryan GH, Wyngaard JC, Fritsch JM. 2003. Resolution requirements for the simulation of deep moist convection. *Mon. Weather Rev.* **131**: 2394–2416.
- Colella P, Woodward PR. 1984. The Piecewise Parabolic Method (PPM) for gas-dynamical simulations. *J. Comput. Phys.* **54**: 174–201.
- Couvreux F, Rio C, Guichard F, Lothon M, Canut G, Bouniol D, Gounou A. 2012. Initiation of daytime local convection in a semi-arid region analysed with high-resolution simulations and AMMA observations. *Q. J. R. Meteorol. Soc.* **138**: 56–71.
- Cuxart J, Jiménez M. 2007. Mixing processes in a nocturnal low-level jet: An LES study. *J. Atmos. Sci.* **64**: 1666–1679.
- Cuxart J, Bougeault P, Redelsperger JL. 2000. A turbulence scheme allowing for mesoscale and large-eddy simulations. *Q. J. R. Meteorol. Soc.* **126**: 1–30.
- Davies T, Cullen MJP, Malcolm AJ, Mawson MH, Staniforth A, White AA, Wood N. 2005. A new dynamical core for the Met Office's global and regional modelling of the atmosphere. *Q. J. R. Meteorol. Soc.* **131**: 1759–1782.
- Dirmeyer PA, Cash BA, Kinter JL, Jung T, Marx L, Satoh M, Stan C, Tomita H, Towers P, Wedi N, Achuthavarier D, Adams JM, Altshuler EL, Huang B, Jin EK, Manganello J. 2012. Simulating the diurnal cycle of rainfall in global climate models: Resolution versus parametrization. *Clim. Dyn.* **39**: 399–418.
- Durran DR. 1989. Improving the anelastic approximation. *J. Atmos. Sci.* **46**: 1453–1461.
- Fiori E, Parodi A, Sicardi F. 2009. Dealing with uncertainty: Turbulent parametrizations and grid-spacing effects in numerical modelling of deep moist convective processes. *Nat. Hazards Earth Syst. Sci.* **9**: 1871–1880.
- Fiori E, Parodi A, Sicardi F. 2010. Turbulence closure parametrization and grid spacing effects in simulated supercell storms. *J. Atmos. Sci.* **67**: 3870–3890.
- Fovell RG, Mullendore GL, Kim SH. 2006. Discrete propagation in numerically simulated nocturnal squall lines. *Mon. Weather Rev.* **134**: 3735–3752.
- Gal-Chen T, Somerville RC. 1975. On the use of a coordinate transformation for the solution of the Navier–Stokes equations. *J. Comput. Phys.* **17**: 209–228.
- Hirahara YJ, Ishimizu T. 2011. Trial operation of the local forecast model at JMA. *CAS/JSC WGNE Res. Act. Atmos. Ocean Model.* **41**: 5.11–5.12.
- Honnert R, Masson V, Couvreux F. 2011. A diagnostic for evaluating the representation of turbulence in atmospheric models at the kilometric scale. *J. Atmos. Sci.* **68**: 3112–3131.
- Houze RAJ. 1993. *Cloud Dynamics, International Geophysics* **53**. Academic Press: San Diego, CA.
- Janjic ZI. 2003. A non-hydrostatic model based on a new approach. *Meteorol. Atmos. Phys.* **82**: 271–285.
- Kain JS, Weiss SJ, Bright DR, Baldwin ME, Levitt JJ, Carbin GW, Schwartz CS, Weisman ML, Droegeemeier KK, Weber DB, Thomas KW. 2008. Some practical considerations regarding horizontal resolution in the first generation of operational convection-allowing NWP. *Weather and Forecasting* **23**: 931–952.
- Khairoutdinov MF, Krueger SK, Moeng CH, Bogenschutz P, Randall DA. 2009. Large-eddy simulation of maritime deep tropical convection. *J. Adv. Model. Earth Syst.* **1**: 15, doi: 10.3894/JAMES.2009.1.15.
- Klemp JB, Wilhelmson RB. 1978. The simulation of three-dimensional convective storm dynamics. *J. Atmos. Sci.* **35**: 1070–1096.
- Krauss TW, Marwitz JD. 1984. Precipitation processes within an Alberta supercell hailstorm. *J. Atmos. Sci.* **41**: 1025–1035.
- Lafore JP, Stein J, Asencio N, Bougeault P, Ducrocq V, Duron J, Fischer C, Héreil P, Mascart P, Masson V, Pinty JP, Redelsperger JL, Richard E, Vilà-Guerau de Arellano J. 1997. The Meso-NH atmospheric simulation system. Part I: Adiabatic formulation and control simulations. *Ann. Geophys.* **16**: 90–109.
- Langhans W, Schmidli J, Schär C. 2012. Bulk convergence of cloud-resolving simulations of moist convection over complex terrain. *J. Atmos. Sci.* **69**: 2207–2228.
- Lean HW, Clark PA, Dixon M, Roberts NM, Fitch A, Forbes R, Halliwell C. 2008. Characteristics of high-resolution versions of the Met Office Unified Model for forecasting convection over the United Kingdom. *Mon. Weather Rev.* **136**: 3408–3424.
- Lemon LR, Doswell CA. 1979. Severe thunderstorm evolution and mesocyclone structure as related to tornadogenesis. *Mon. Weather Rev.* **107**: 1184.
- Lilly DK. 1986. The structure, energetics and propagation of rotating convective storms. Part II: Helicity and storm stabilization. *J. Atmos. Sci.* **43**: 126–140.
- Mesinger F, Arakawa A. 1976. 'Numerical methods used in atmospheric models', Technical Report, vol. 1, GARP Publications Series No. 17. WMO/ICSU Joint Organizing Committee: Geneva, Switzerland.
- Moeng CH, Sullivan PP, Khairoutdinov MF, Randall DA. 2010. A mixed scheme for subgrid-scale fluxes in cloud-resolving models. *J. Atmos. Sci.* **67**: 3692–3705.
- Narita M, Ohmori S. 2007. Improving precipitation forecasts by the operational non-hydrostatic mesoscale model with the Kain–Fritsch convective parametrization and cloud microphysics. *Preprints, 12th Conference on Mesoscale Processes*, paper 3.7, Waterville Valley, NH. American Meteorological Society: Boston, MA.
- Parodi A, Tanelli S. 2010. Influence of turbulence parametrizations on high-resolution numerical modeling of tropical convection observed during

- the TC4 field campaign. *J. Geophys. Res.* **115**: D00J14, doi: 10.1029/2009JD013302.
- Petch J, Brown A, Gray M. 2002. The impact of horizontal resolution on the simulations of convective development over land. *Q. J. R. Meteorol. Soc.* **128**: 2031–2044.
- Pierrehumbert RT. 1984. Local and global baroclinic instability of zonally varying flow. *J. Atmos. Sci.* **41**: 2141–2162.
- Pinty JP, Jabouille P. 1998. A mixed-phase cloud parametrization for use in mesoscale non-hydrostatic model: Simulations of a squall line and of orographic precipitations. *Proceedings Conference of Cloud Physics*, Everett WA, 217–220. American Meteorological Society: Boston, MA.
- Redelsperger JL, Sommeria G. 1981. Méthode de représentation de la turbulence d'échelle inférieure à la maille pour un modèle tri-dimensionnel de convection nuageuse. *Boundary Layer Meteorol.* **21**: 509–530.
- Redelsperger J, Sommeria G. 1986. Three-dimensional simulation of a convective storm: Sensitivity studies on subgrid parametrization and spatial resolution. *J. Atmos. Sci.* **43**: 2619–2635.
- Ricard D, Lac C, Riette S, Legrand R, Mary A. 2013. Kinetic energy spectra characteristics of two convection-permitting limited-area models AROME and Meso-NH. *Q. J. R. Meteorol. Soc.* **139**: 1327–1341.
- Rotunno R. 1981. On the evolution of thunderstorm rotation. *Mon. Weather Rev.* **109**: 577–586.
- Rotunno R, Klemp JB. 1982. The influence of the shear-induced pressure gradient on thunderstorm motion. *Mon. Weather Rev.* **110**: 136–151.
- Saito K, Fujita T, Yamada Y, Ishida Ji, Kumagai Y, Aranami K, Ohmori S, Nagasawa R, Kumagai S, Muroi C, Kato T, Eito H, Yamazaki Y. 2006. The operational JMA non-hydrostatic mesoscale model. *Mon. Weather Rev.* **134**: 1266–1298.
- Seity Y, Brousseau P, Malardel S, Hello G, Bénard P, Boutrier F, Lac C, Masson V. 2011. The AROME–France convective-scale operational model. *Mon. Weather Rev.* **139**: 976–991.
- Seity Y, Ricard D, Léger J, Pietrissi M. 2014. Evaluation of increased horizontal and vertical resolutions in AROME–France deterministic forecasts for convective events. *ALADIN–HIRLAM Newslett.* **2**: 16–19. <http://www.cnrm.meteo.fr/aladin/spip.php?article260> (accessed 22 April 2014).
- Skamarock WC. 2004. Evaluating mesoscale NWP models using kinetic energy spectra. *Mon. Weather Rev.* **132**: 3019–3032.
- Skamarock WC, Klemp JB. 2008. A time-split non-hydrostatic atmospheric model for weather research and forecasting applications. *J. Comput. Phys.* **227**: 3465–3485.
- Stout G, Huff F. 1953. Radar records Illinois tornadogenesis. *Bull. Am. Meteorol. Soc.* **34**: 281–284.
- Takemi T, Rotunno R. 2003. The effects of subgrid model mixing and numerical filtering in simulations of mesoscale cloud systems. *Mon. Weather Rev.* **131**: 2085–2101.
- Warren RA, Kirshbaum DJ, Plant RS, Lean HW. 2013. A ‘Boscawen-type’ quasi-stationary convective system over the UK Southwest Peninsula. *Q. J. R. Meteorol. Soc.* **140**: 240–257.
- Weisman ML, Klemp JB. 1982. The dependence of numerically simulated convective storms on vertical wind shear and buoyancy. *Mon. Weather Rev.* **110**: 504–520.
- Weisman ML, Klemp JB. 1984. The structure and classification of numerically simulated convective storms in directionally varying wind shears. *Mon. Weather Rev.* **112**: 2479–2498.
- Weisman ML, Skamarock WC, Klemp JB. 1997. The resolution dependence of explicitly modeled convective systems. *Mon. Weather Rev.* **125**: 527–548.
- Weisman ML, Davis C, Wang W, Manning KW, Klemp JB. 2008. Experiences with 0–36-h explicit convective forecasts with the WRF–ARW model. *Weather and Forecasting* **23**: 407–437.
- Wyngaard JC. 2004. Toward numerical modeling in the ‘Terra Incognita’. *J. Atmos. Sci.* **61**: 1816–1826.
- Zhang M, Zhang DL. 2012. Subkilometer simulation of a torrential-rain-producing mesoscale convective system in East China. Part I: Model verification and convective organization. *Mon. Weather Rev.* **140**: 184–201.